Modelling and optimization of vacuum pressure swing adsorption CO_2 capture pilot using MIL-160(Al)

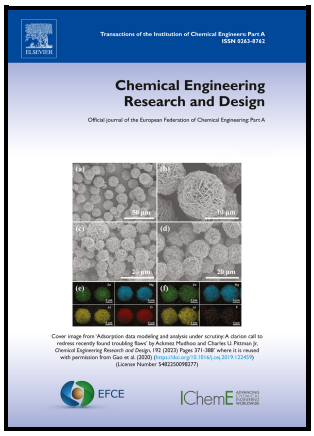

A. Henrotin, N. Heymans, M.-E. Duprez, G. De Weireld

PII: S0263-8762(25)00689-6

DOI: https://doi.org/10.1016/j.cherd.2025.12.030

Reference: CHERD7196

To appear in: *Chemical Engineering Research and Design*

Received date: 3 September 2025
Revised date: 5 December 2025
Accepted date: 16 December 2025

Please cite this article as: A. Henrotin, N. Heymans, M.-E. Duprez and G. De Weireld, Modelling and optimization of vacuum pressure swing adsorption CO_2 capture pilot using MIL-160(Al), *Chemical Engineering Research and Design,* (2025) doi:https://doi.org/10.1016/j.cherd.2025.12.030

Modelling and optimization of vacuum pressure swing adsorption CO_2 capture pilot using MIL-160(Al)

A. Henrotin, N. Heymans, M.-E. Duprez, G. De Weireld*

Thermodynamics and Mathematical Physics Unit, University of Mons (UMONS), Place du parc 20, 7000 Mons, Belgium

* Corresponding author: Email address: guy.deweireld@umons.ac.be

Abstract

Global warming, driven by increasing CO_2 emissions from fossil fuel combustion, necessitates the development of effective carbon capture technologies. Among various approaches, Vacuum Pressure Swing Adsorption (VPSA) offers an energy-efficient solution for post-combustion CO_2 capture, especially in power plants and energy-intensive industries. This work focuses on validating a simulation model using a laboratory VPSA pilot with the Aluminum Metal-Organic Framework (Al-MOF) MIL-160(Al) and optimizing both lab-scale and industrial-scale VPSA pilots through simulation. Process modeling in Aspen Adsorption software simulated a 3-bed 6-step cycle using parameters from experimental adsorption isotherms and breakthrough curves. The simulation model was compared to previous lab-scale VPSA pilot experiments treating a synthetic 15/85 CO_2/N_2 mixture at 1 Nm³/h, showing mean absolute errors of 1.47% for purity and 3.19% for recovery.

Surrogate models, including kriging and artificial neural networks (ANN), were used to optimize recovery and purity of the lab-scale pilot using the Non-dominated Sorting Genetic Algorithm-II (NSGA-II). The ANN model proved more accurate, especially in determining pareto fronts. The model was extended to an industrial VPSA pilot as part of the MOF4AIR project, designed to treat flue gas of 50 to 100 Nm³/h with three 41 L adsorption columns. Simulations showed that the pilot could achieve 95% purity and recovery for CO_2 concentrations ranging from 5 to 15%. The estimated energy consumption and productivity for 15% CO_2 gas were 413.19 kWh/tCO_2 and 3.03 tCO_2/(m³ads.day) at a gas flow rate of 55.62 Nm³/h, demonstrating the technology's potential and competitiveness on a larger scale.

Keywords

CO_2 capture; Vacuum pressure swing adsorption; Metal organic framework; Surrogate; Optimization

1 Introduction

In 2024, global surface temperature has been increased by +1.55°C above pre-industrial levels, driven by greenhouse gas emissions—requiring a 48% cut in CO_2 by 2030 and net-zero by 2050 to limit warming to 2°C, as climate impacts like extreme weather and ocean acidification intensify (Calvin et al., 2023; WMO, 2024). To reach these global targets, several measures must be implemented, including transitioning from fossil fuels without CCS (Carbon Capture and Storage) to very low or zero-carbon energy sources such as renewable or fossil fuels with carbon capture, improving energy efficiency, reducing energy consumption, and reducing non-CO_2 GHG emissions. In transition phase or for specific sectors CCS is highlighted as a crucial element of the solution, particularly with unavoidable emissions in industrial sectors such as cement, lime and steel production or petroleum refining where a part of the CO_2 emissions comes from chemical reactions (Bains et al., 2017; Calvin et al., 2023). CCU

(Carbon Capture and utilization) is also an alternative pathway to the storage of carbon dioxide. (Chauvy & De Weireld, 2020; Hong, 2022; IEA, 2020).

Post-combustion carbon capture involves separating the CO_2 from flue gas generated by fossil fuel combustion or chemical processes (*e.g.* boilers, industrial furnaces, cement kilns, blast furnaces). Different technologies exist for this purpose. Among them, chemical absorption with amines is the most mature technology (TRL9) but suffers from energy penalties due to high energetic consumption, solvent degradation, solvent loss, and high corrosiveness (N.Borhani & Wang, 2019). Alternatives to absorption techniques include membrane separation, cryogenic distillation, chemical looping, biological processes with microalgae, adsorption or a combination of these (Costa, Coppitters, et al., 2024; Costa, Henrotin, et al., 2024; Mondal et al., 2012; Sifat & Haseli, 2019). In adsorption processes, the separation is made by either changing the temperature (TSA: Temperature Swing Adsorption) or varying the pressure (PSA: Pressure Swing Adsorption) depending on CO_2 concertation in flue gas (Spigarelli & Kawatra, 2013; Wilberforce et al., 2021). Various types of adsorbents are used, including activated carbons, zeolites, silica membranes, or, more recently, metal organic frameworks (Wilberforce et al., 2021). Separation of gases by adsorption is already used in numerous fields such as air separation, H_2 purification, biogas upgrading, etc. but need more development to be used for CO_2 capture (Riboldi & Bolland, 2017; Ruthven, 1984; Yang, 1987). VPSA processes are preferred to PSA for CO_2 capture as the use of vacuum is more economical since the flus gas to treat is already at atmospheric pressure, allowing to compress smaller gas flows (product stream) compared to PSA process (feed stream) (Grande, 2012).

The benchmark material for CO_2 capture in flue gases through adsorption is zeolite 13X, a porous aluminosilicate material. At 25°C and a pressure of 1 bar, its reported CO_2 adsorption capacity for a 15/85 CO_2/N_2 mixture is comprised between 2.5 and 3.8 mmol/g and a selectivity of CO_2 over N_2 between 100 and 700 (Chue et al., 1995; Hu et al., 2019b). However, zeolites are sensitive to water which reduces drastically their CO_2 adsorption capacity and active surface area, and to contaminants such as SO_X and NO_X. (Bahamon et al., 2018; Raganati et al., 2021). As an alternative, Metal Organic Frameworks (MOFs) have gained attention as a promising class of adsorbents for carbon capture over the past two decades. They exhibit microporous crystalline structures composed of central cation molecules (metal atoms or cluster) linked together by organic ligands (coordinate bonds) to form one, two or three-dimensional networks (Spigarelli & Kawatra, 2013). The large number of MOFs that can be synthesized results in materials exhibiting high adsorption capacity, high selectivity for CO_2 versus N_2, finely tunable pore surface properties, and scalability for industrial applications (Spigarelli & Kawatra, 2013). Among these, Mg-MOF-74 has one of the highest CO_2 adsorption capacities, giving 5.9 mmol/g for a pressure of 1 bar, 15/85 CO_2/N_2 mixture and 25°C, and a CO_2/N_2 selectivity of 182 in the same conditions. Higher selectivity can be obtained with other MOFs such as the UTSA-16 (selectivity of 315) but with a lower adsorption capacity (2.06 mmol/g) for the same conditions as Mg-MOF-74 (Ding et al., 2019; Hu et al., 2019; Younas et al., 2020). Mg-MOF-74 exhibits a high heat of adsorption (-47 to -52 kJ/mol) while the UTSA-16 has a moderate heat of adsorption of -34.6 kJ/mol. Mg-MOF-74 has been reported to be sensitive to water decreasing the CO_2 capacity and degrading the crystalline structure when exposed during one day to water (Decoste et al., 2013; Hu et al., 2019). This MOF is also sensitive to SO_2 and NO_2 poisoning the adsorption sites due to high bounding energy (Tan et al., 2017; J. Yu & Balbuena, 2013). UTSA-16 presents also a decrease of CO_2 adsorption capacity in the presence of water but without degradation of the microstructure (Masala et al., 2017). The presence of SO_2 or NO_2 in the flue gas also reduces the CO_2 adsorption capacity of the adsorbent (Gaikwad et al., 2020). One of the most interesting MOFs for CO_2 capture is the Calgary Framework 20 (CALF-20), exhibiting high capacity (2.75 mmol/g for 0.15 bar of CO_2 at 20°C on the powder), high selectivity (230

for a 10/90 CO_2 /N_2 mixture) even in presence of water pressure vapor, moderate heat of adsorption (-39 kJ/mol), stability over steam and acid gases. The raw materials needed for the production of this MOF are commercially available and the pathway of production can easily be applied in industry, showing a good scalability of this MOF for the industrial CO_2 capture (Lin et al., 2021).

The adsorbent scale properties (adsorption capacity, selectivity, heat of adsorption, etc.) and metrics using its properties such as Notaro, Ackley, Yang, Wiersum, etc. provide a way to screen the most promising adsorbents for CO_2 capture but are not sufficient to evaluate the performance of the adsorbent in adsorption cycle for CO_2 capture process (Khurana & Farooq, 2016a; Rajagopalan et al., 2016). These processes are usually evaluated by the recovery and purity of CO_2 which must be higher than 95% as recommended by the by the U.S. Department of Energy to be efficient (NETL, 2023). Two additional metrics, energy consumption and productivity, are also evaluated in a process to compare economic competitiveness with other CO_2 capture technologies (Grande, 2012). Process evaluation is made by either simulation or pilot experiments, this last option required enough adsorbent to be tested, in addition to high cost and time consumption. However, testing new material in realistic condition is crucial to validate the simulations made. Simulation of adsorption process allows to evaluate a material with parameters (adsorption isotherms, kinetic, geometry) which can be obtained from relatively small scale (a few dozen grams) and optimize the process to find the pareto front of energy/productivity for a recovery and purity higher than 95%. Nevertheless, simulations are relatively complex because of the need to simulate the dynamic behavior of the adsorption column for a sufficiently long time to reach steady state, resulting in runs that can last several hours (Farmahini et al., 2021; Haghpanah et al., 2013).

Numerous adsorbents have been tested by simulations with different VPSA cycle configurations. Activated carbon, zeolite 13X, Mg-MOF-74, UTSA-16 and CALF-20 have been tested for a dry 15/85 CO_2/N_2 flue gas with the 4-step cycle composed of adsorption, co-current evacuation, counter-current evacuation, and light product pressurization. This cycle can achieve up to 95% purity and 90% recovery simultaneously. Best results are obtained with UTSA-16 with an energy consumption ranged from 116–120 kWh/tCO_2, and productivity between 2.18–2.81 $tCO_2/(m^3 \cdot day)$. However, the required 0.03 bar for the evacuation step is difficult to implement at industrial level. (Nguyen et al., 2022; Rajagopalan et al., 2016). This cycle was also tested experimentally with 13X and CALF-20 in different works confirming the simulation accuracy, with mean errors between 1.16% and 2.7% for purity and recovery (Estupiñan Perez et al., 2019; Krishnamurthy et al., 2014; Nguyen et al., 2023). Silica gel was also tested experimentally on a PSA pilot using a dual-reflux cycle (composed of adsorption, equalization, evacuation, light and heavy reflux steps) with a 15/85 CO_2/N_2 mixture giving 99.18% purity and 99.62% recovery. By simulation the energy consumption was estimated to 538 kWh/t_{CO2} for a productivity of 3.17 $t_{CO2}/(m^3.day)$ (Li et al., 2016). Other cycle simulations have been validated with experimental data obtained on apparatus composed of a single column such as the Skarstrom cycle (adsorption, evacuation, light reflux, pressurization) with activated carbon and zeolite 13X or 3-bed 7-step cycles (adsorption, co-current evacuation, heavy reflux, pressure equilibrium, co-current evacuation, light reflux, and second pressure equilibrium) with zeolite 5A . Simulation results are in good agreement with experiments but only a qualitative comparison was made (Liu et al., 2012; Shen et al., 2011; L. Wang et al., 2012). Table S1 in Supporting Information provides more information about the VPSA discussed in this introduction.

Simulation of VPSA process can be also used as a screening tool to identify the best adsorbent for a given cycle or the best operating conditions for a given process. Genetic algorithm such as the Non-Dominated Sorting Genetic Algorithm II (NSGA-II) (Deb et al., 2002) or NSGA-III (Deb & Jain, 2014) are commonly used for multi-objective optimization balancing trade-offs like purity-recovery and energy

consumption in VPSA simulations (Estupiñan Perez et al., 2019; Haghpanah et al., 2013; Khurana & Farooq, 2016b; Nguyen et al., 2023). These algorithms efficiently explore Pareto fronts but require hundreds to thousands of simulations (Kudela & Matousek, 2022). In surrogate modelling, a simpler mathematical model is constructed with a limited number of simulated data. Kriging model has been used for optimization of cycles reducing the number of simulations by 2 to 5 compared to direct optimization (Beck et al., 2015). Adaptive kriging can further enhance precision by iteratively refining the model with additional simulation points during optimization (Alkebsi & Du, 2021).

Another popular surrogate model used in VPSA simulation is artificial neural network (ANN). Several works compare results obtained with process optimization using a full model compared to optimization with ANN ~~a~~n 8-step PSA cycle for H_2/CO_2 separation was optimized, showing that only 1122 simulations were required to construct an ANN model with 8 decision variables reducing the simulation time required by 10 compared to traditional optimization (Subraveti et al., 2019). For pre-combustion CO_2 capture, an ANN built with 18,000 simulations closely matched full-model results, though accuracy declined at the edges of the sampling domain (Streb & Mazzotti, 2022). For post-combustion capture, ANN models have accurately optimized multi-step VPSA cycles e.g., a 3-bed, 7-step silica-gel process trained with 2,000 simulations achieving $R^2 > 99\%$ (Z. Wang et al., 2022). ANN model can also be used to model a single step of a VPSA cycle, allowing to synthesize new cycle. This methodology was successfully applied to zeolite 13X and Ni-MOF-74 for the simulation of a 3-step cycle, Skarstrom cycle and 5-step cycle (Leperi et al., 2019).

ANNs also enable virtual adsorbent screening by incorporating isotherm. This methodology has been applied to the 5-step cycle (adsorption, co and counter-current evacuation, light reflux, light product pressurization) with a dual-site Langmuir isotherm, identifying materials such as h8155527 (hypothetic zeolitic structure), IISERP-MOF2 (hypothetical MOF) or UTSA-16 as the most promising to reduce the energy consumption and increase the productivity (Khurana & Farooq, 2016a; Pai et al., 2021). However, this method remains approximate because it uses only one type of isotherm, macropore diffusion as the single mass transfer resistance and constant adsorbent characteristics (c_p, density, size, etc.) without being based on actual measurements for the tested adsorbents.

In this work, the performance of the MIL-160(Al) in process conditions are studied by simulation. This MOF has been experimentally tested in our previous work with a laboratory scale pilot performing a 3-bed 6-step cycle (adsorption, heavy reflux, co and counter-current evacuation, light reflux, light product pressurization) giving a purity of 90% and recovery of 92.7% for the separation of a 15/85 CO_2/N_2 mixture with a moderate level of vacuum (0.1 bar) (Henrotin et al., 2024). MIL-160(Al) exhibits numerous advantages such as high surface area and pore volume (1220 m^2/g and 0.404 cm^3/g respectively), a CO_2 working capacity at 30°C of 0.85 mmol/g for partial pressures between 0.15 and 0.015 bar, a relatively low heat of adsorption (-33 kJ/mol for CO_2), an IAST CO_2/N_2 selectivity at 1 bar and 30°C of 34 for a 15/85 mixture,a resistance in presence of water, and a green path for the production of this MOF at kg scale, making it a promising candidate for post-combustion CO_2 capture (Damasceno Borges et al., 2017; Permyakova et al., 2017; Severino et al., 2021; Wahiduzzaman et al., 2018). This MOF was studied experimentally and by simulation for biogas upgrading showing interesting properties for the CO_2/N_2 and CO_2/CH_4 separation such as the fast kinetic of adsorption or the low heat of regeneration. Measurement on a laboratory scale PSA pilot for the CO_2/CH_4 separation was performed with simulation of the results obtained showing a good agreement between the experiments and modelling (Karimi et al., 2023, 2024).

A simulation model was developed in this work to simulate the 3-bed 6-step cycle with MIL-160(Al) and is compared to the experimental results obtained on the lab-scale pilot. The simulation model is then used to find the pareto fronts (recovery-purity and energy-productivity) of the VPSA pilot with a

comparison between the direct optimization of the complete model and the use of surrogate models to reduce the computation time. Two models which have been used for approximating VPSA simulation were compared in this work: kriging and ANN. The accuracy and the number of simulations required were studied with the lab-scale VPSA simulation model to determine the best surrogate model. The validated model is finally used to determine operating conditions of the industrial pilot of the H2020-MOF4AIR project, located at the Technology Centre Mongstad (TCM) test site with data obtained at laboratory scale. This pilot is composed of three adsorption columns of 41 L to capture CO_2 from 50 to 100 Nm^3/h of flue gas coming from a residual fluid catalytic cracking unit (RFCC) containing around 14% of CO_2 or a process furnace containing 4 to 15% of CO_2 (Heymans et al., 2021). Optimization of energy consumption and productivity while reaching the target of CO_2 capture process (recovery and purity >95%) was performed for different flue gas compositions.

2 Materials and methods

2.1 Experimental measurements

2.1.1 Materials

The MOF studied in this work is the MIL-160(Al) (Formula: $Al(OH)(O_2C–C_4H_2O–CO_2)$) formed by aluminum chains linked via five-membered ring 2,5 furan di-carboxylate ligand, giving a helical shape with pore diameters ranging from 4 to 6 Å. This material exhibits interacting sites for CO_2 or H_2O giving a good selectivity of CO_2 over N_2 (Cadiau et al., 2015; Damasceno Borges et al., 2017). This MOF has been reported to be resistant to water (Permyakova et al., 2017) and SO_2 with no structural degradation, although it shows a preferential adsorption of SO_2 compared to CO_2 (Brandt et al., 2019). However, molecular simulations have indicated that the material degrades upon exposure to H_2S (Lyu & Maurin, 2021).

In this study, MIL-160(Al) was synthesized and shaped by MOF Technologies using extrusion techniques, resulting in a cylindrical form. A total of 60 kg was produced for use in an industrial pilot in the demonstration site as part of the MOF4AIR project. An aliquot of this batch was sampled for testing at laboratory scale. The geometrical properties of the material were determined using a caliper (accuracy of 0.01 mm) and a scale (accuracy of 10^{-4} g) on 20 pellets. The pellets have a cylindrical shape, with a mean diameter of 2.07 mm and a mean length of 4.20 mm. The measured pellet density is 554.65 kg/m^3.

2.1.2 Adsorption isotherms

The CO_2 adsorption isotherms were measured over a pressure range of 0.01 to 1 bar, while the N_2 adsorption isotherms were measured from 0.1 to 50 bar using a gravimetric device (Billemont et al., 2017). This wide pressure range allows the application of the ideal adsorbed solution theory (IAST) under optimal conditions, where calculating the adsorbed amount requires extrapolating to lower pressures for the most adsorbed compound and to higher pressures for the less adsorbed one (Billemont et al., 2017; Myers & Prausnitz, 1965). More information can be found in our previous paper (Henrotin et al., 2024).

2.1.3 Breakthrough curves

Breakthrough curves experiments were performed to determine adsorption kinetics and adjust the parameters of the heat transfer correlations used (see Section 2.2.2). Column of 30 cm height and 7.01 cm diameter was filled with the MIL-160(Al) and regenerated overnight at room temperature under vacuum (typical lowest pressure of the vacuum pump: 2 Pa). The column was then pressurized with pure nitrogen until temperatures inside the column were stabilized. The CO_2/N_2 gas mixture used for breakthrough curve measurements was generated using two thermal mass flow controllers.

During a breakthrough curve, the gas was sent to the bottom of the column and the outlet composition was continuously monitored using a NDIR analyzer. The temperature profile during the experiment was recorded with two type K thermocouples placed inside an immersion sleeve at 5 cm and 25 cm from the bottom of the adsorption layer. Different flow rates (0.3 to 1 Nm³/h) and CO_2 concentrations (10 to 50%) were tested to separate kinetics from thermal effects. Breakthrough curve measurement lasted 30 minutes, followed by a 30 min desorption phase using pure nitrogen at the same flow rate.

2.1.4 Vacuum pressure swing adsorption cycles

The performance of MIL-160(Al) was evaluated using a home-made vacuum pressure swing adsorption pilot (Henrotin et al., 2024). Three columns, identical to the column used for breakthrough curve measurements, were filled with MIL-160(Al). A set of valves allow to direct the gas flow into different sections of the pilot to perform the different steps of a VPSA cycle (adsorption, evacuation, reflux, …) and therefore potentially all the cycles using two or three columns.

The cycle studied is the 6-step cycle described by Khurana & Farooq, (2016b), which includes adsorption, heavy reflux, co-current evacuation, counter-current evacuation, light reflux, and light product pressurization. The cycle was adapted for a 3-column configuration and the different steps of the cycle are represented in Figure 1. This cycle is able to provide good separation performance with a moderate level of vacuum (0.1 bar) which is realistic for industrial applications. The performance of MIL-160(Al) had already been assessed in previous work (Henrotin et al., 2024), showing better results compared to the benchmark material, zeolite 13X.

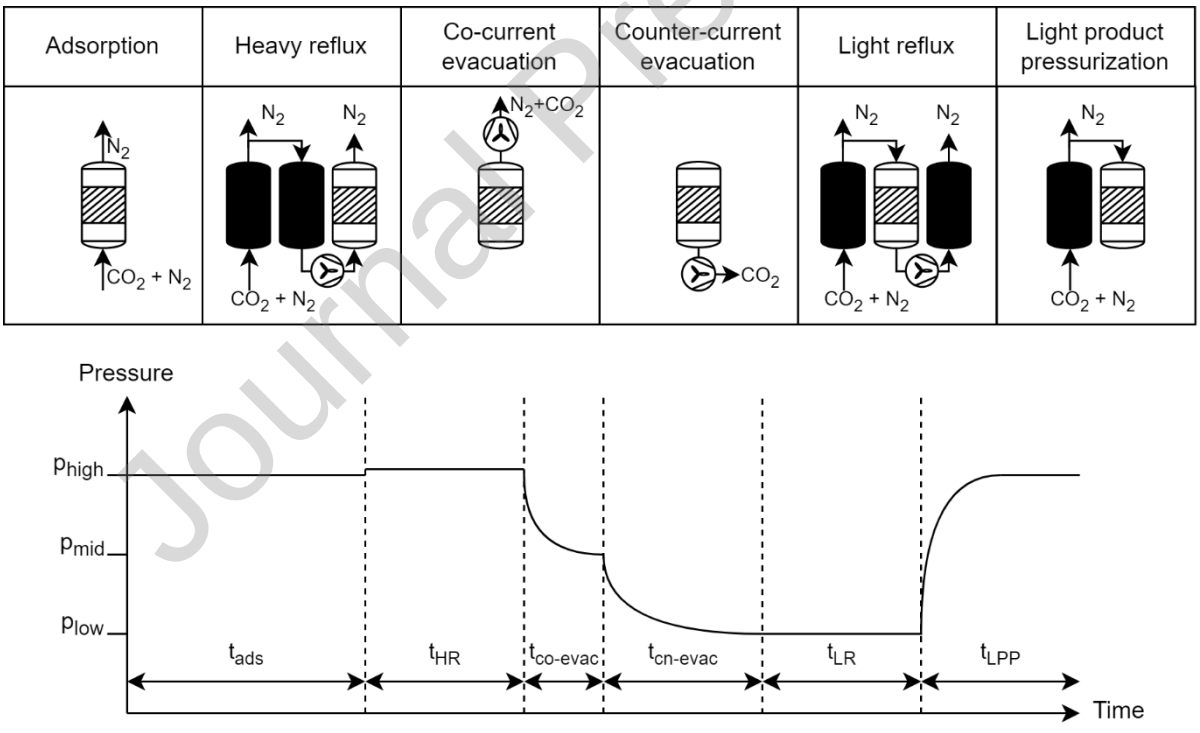

Figure 1: Representation of the different steps of the 3-bed 6-step cycle with pressure level representation of bed 1 (HR: heavy reflux, co-evac: co-current evacuation, cn-evac: counter-current evacuation, LR: light reflux, LPP: light product pressurization).

The duration of each step can be defined by three variables when three adsorption beds are used. Adsorption time, light reflux time, and co-current evacuation time were chosen to define the cycle. The remaining step durations are determined using equations (1) to (3). The pressure levels of adsorption, co-current evacuation and counter-current evacuation and the flow rate of the flue gas, and the flow rate of light reflux are additional variables of the VPSA process.

$$t_{heavy\ reflux} = t_{light\ reflux} \quad (1)$$

$$t_{counter-current\ evacuation} = t_{adsorption} - t_{light\ reflux} - t_{co-current\ evacuation} \quad (2)$$

$$t_{light\ product\ pressurization} = t_{adsorption} - t_{light\ reflux} \quad (3)$$

The performance of the cycle is determined using four indicators: purity, recovery, productivity, and energy consumption (Grande, 2012). Purity represents the CO_2 concentration at the outlet of the VPSA process. Since flow rate and concentration vary during one cycle, an average value is computed using equation (4). Recovery expresses the quantity of CO_2 recovered at the VPSA outlet relative to the CO_2 amount in the flue gas to be treated, as defined in equation (5).

Productivity is an image of the material's efficiency giving the amount of CO_2 recovered per volume of adsorbent for a given time (typically one hour or one day). This indicator (equation (6)) gives an idea of the gas flow rate that can be treated per cubic meter of adsorbent or the VPSA unit size required for a given flow rate. Finally, energy consumption is the amount of energy required to obtain one ton of CO_2 at the VPSA outlet, as defined in equation (7) where E is the energy consumption per cycle for the vacuum pump or compressor.

$$Purity\ [\%] = \frac{\sum_{cycle} Q_{product} y_{CO_2\ product}}{\sum_{cycle} Q_{product}} \quad (4)$$

$$Recovery\ [\%] = \frac{\sum_{cycle} Q_{product} y_{CO_2\ product}}{\sum_{cycle} Q_{feed} y_{CO_2\ feed}} \quad (5)$$

$$Productivity\ \left[t_{CO_2}/(m^3.day)\right] = \frac{\sum_{cycle} Q_{product} y_{CO_2\ product}}{V_{ads}.t_{cycle}} \quad (6)$$

$$Energy\ consumption\ \left[kWh/t_{CO_2}\right] = \frac{\sum E}{\sum_{cycle} Q_{product} y_{CO_2\ product}} \quad (7)$$

$$E\ [kWh] = \sum_{cycle} \frac{Q.R.T}{\eta} \frac{\gamma}{\gamma - 1} \left(\left(\frac{p_2}{p_1} \right)^{\frac{\gamma-1}{\gamma}} - 1 \right) \quad (8)$$

With Q the molar flow rate, y the molar fraction, V_{ads} the volume of adsorbent used, t_{cycle} the time of one cycle, R the gas constant, T the temperature, η the isentropic efficiency, γ the heat capacity ratio, p_1 the inlet pressure and p_2 the outlet pressure.

2.2 Modeling

2.2.1 Adsorption isotherms

The experimental adsorption isotherms obtained using the methodology described in Section 2.1.2 were modelled to predict the adsorbed amounts at different temperatures and partial pressures. A Langmuir model with temperature dependency (equation (9)) was used to fit experimental data for pure CO_2 and pure nitrogen using the same saturation capacity (q_s) for both gases (Do, 1998; Langmuir, 1918; Ruthven, 1984). The nonlinear least-squares method using the trust region reflective algorithm was used within Matlab© software (lsqnonlin function) to determine the parameters of the model. The algorithm minimizes the cost function, defined as the sum of squared differences between the measured and modeled adsorbed amounts with the parameters to be identified. Moreover, a multistart procedure was applied to initialize the optimization procedure with various starting conditions to avoid convergence to local minimum. The 95% confidence intervals of the parameters were calculated using the Jacobian matrix provided by the solver (Tolazzi et al., 2018). The adsorbed amount for a CO_2/N_2 mixture was computed using two methods which are compared: (i) The Ideal Adsorbed Solution Theory (IAST) using the Langmuir model (equation (9)) to represent pure

component adsorption isotherms, as described in Section 2.1 of the Supporting Information (Billemont et al., 2017; Myers & Prausnitz, 1965), and (ii) the extended Langmuir model for mixture (Do, 1998; Ruthven, 1984) defined by equation (10). The heat of adsorption (ΔH) was determined using the Clausius-Clapeyron method by fitting the experimental data with Langmuir model (Do, 1998).

$$q = q_s \frac{b_0 \exp\left(-\frac{\Delta H}{RT}\right) p}{1 + b_0 \exp\left(-\frac{\Delta H}{RT}\right) p} \tag{9}$$

$$q_i = q_s \frac{b_{0,i} \exp\left(-\frac{\Delta H_i}{RT}\right) p_i}{1 + \sum_j b_{0,j} \exp\left(-\frac{\Delta H_j}{RT}\right) p_j} \tag{10}$$

R^2 (coefficient of determination) and the normalized root mean squared deviation (NRMSD) (equations (11) and (12)) are used to assess the accuracy of the model in fitting the experimental data. R^2 provides an overall score of the fitting expressed as a percentage while NRMSD quantifies the magnitude of error, also expressed as a percentage (Tolazzi et al., 2018). Therefore, a strong correlation between the model and experimental data is obtained when a high R^2 value is combined with a low NRMSD.

$$R^2 = \frac{\sum_i^n \left(q_{exp,i} - q_{model,i}\right)^2}{\sum_i^n \left(q_{exp,i} - q_{mean}\right)^2} \tag{11}$$

$$NRMSD = \frac{\sqrt{\frac{\sum_i^n \left(q_{exp,i} - q_{model,i}\right)^2}{n}}}{q_{exp,max} - q_{exp,min}} \tag{12}$$

2.2.2 Breakthrough curves

The adsorption bed was modeled using Aspen Adsorption © V14 software to determine the mass transfer coefficients of CO_2 and N_2 and to adjust the heat transfer coefficients. The gas phase properties (compressibility, enthalpy, …) were calculated using the Peng-Robinson equation of state using Aspen Properties © V14 software embedded in Aspen Adsorption. The adsorption bed was divided into 30 axial nodes using the Van Leer scheme (Versteeg & Malalasekera, 2007) to compute the mass, momentum, and thermal balance across the bed. The gas flow through the bed was represented by the axial dispersed plug flow model (equation (13)), assuming no radial effects. The dispersion coefficient was computed using equation (14) for CO_2 and N_2 applying the Chapman-Enskog equation to determine the molecular diffusion coefficient (full model in Section 2.2. of the Supporting Information) (Edwards & Richardson, 1968; Poling et al., 2001; Ruthven, 1984).

$$-D_{L,i} \frac{\partial^2 c_i}{\partial z^2} + \frac{\partial (v c_i)}{\partial z} + \frac{\partial c_i}{\partial t} + \left(\frac{1 - \varepsilon_b}{\varepsilon_b}\right) \frac{\partial q_i}{\partial t} = 0 \tag{13}$$

$$D_{L,i} = \frac{D_m}{\tau_b} + \frac{v\, d_p}{Pe'_\infty \left(1 + \frac{13 D_m}{\tau_b v d_p}\right)} \tag{14}$$

With $D_{L,I}$ the axial diffusion coefficient for compound i, c_i the gas phase concentration for compound i, z the axial distance, v the gas velocity, t the time, ε_b the bed porosity, q_i the adsorbed amount for compound i, D_m the molecular diffusivity, τ_b the bed tortuosity, d_p the volume equivalent spherical diameter of the pellet, and Pe'_∞ the limiting Peclet number.

The pressure drops across the bed was computed using the Ergun equation, which combines the Blake-Kozeny and Burke-Plummer equations, and is valid for a wide range of Reynolds numbers (from

10^{-1} to 10^{5}). The equation is expressed in differential form by equation (15) (Byron Bird et al., 2002; Ergün, 1952).

$$\frac{dp}{dz} = 150\left(\frac{\mu v_0}{d_p^2 \phi_{ads}^2}\right)\frac{(1-\varepsilon_b)^2}{\varepsilon_b^3} + \frac{7}{4}\left(\frac{\rho v_0^2}{d_p \phi_{ads}}\right)\frac{1-\varepsilon_b}{\varepsilon_b^3} \tag{15}$$

With p the pressure, μ the dynamic viscosity, v_0 the superficial velocity, ϕ_{ads} the shape factor of the adsorbent, and ρ the density. Adsorbed amount in the bed was modelled using the Langmuir model (see Section 3.1 for multicomponent model selection). The mass transfer resistance between the adsorbed and gas phases was described using the linear driving force model (equation (16)) (Ruthven, 1984; Yang, 1987).

$$\frac{\partial q_i}{\partial t} = k_{LDF,i}(q_i^* - q_i) \tag{16}$$

With k_{LDF} the linear driving force coefficient, and q_i^* the equilibrium adsorbed amount. Three energy balances were considered in the bed: energy balance of the adsorbent (i), gas (ii), and wall of the bed (iii). These lead to four heat transfer mechanisms in the adsorption bed: heat transfer between the gas and the adsorbent pellets (i), heat transfer between the gas and the column wall (ii), heat transfer across the column wall (iii), and heat transfer between the outer wall and ambient (iv). Equations (17) to (19) give the three energy balances in the bed (Byron Bird et al., 2002; Ruthven, 1984; Wakao & Kaguei, 1982). Heat transfer coefficient between the solid and gas (h_s) was obtained from Martin, (1978) considering a bypass section of the gas due to the increase of void fraction near the column wall. This correlation is described in Section 2.3. of the Supporting Information and is valid for low thermal Peclet numbers (<100) which can be encountered in gas adsorption processes such as the one studied here. The gas-wall heat transfer coefficient (h_w) was estimated using the Yagi & Kunii, (1960) model (Section 2.4. in the Supporting Information). This correlation uses data from various packed bed with d_p/d_{bed} ratios between 0.02 and 0.17 and Reynolds numbers ranging from 20 to 2000 for different solid shapes. Finally, the heat transfer coefficient between the outer wall and ambient (h_{amb}) was computed using classical heat transfer correlations (Incropera & DeWitt, 1996; Kreith et al., 2011) (see Section 2.5. in the Supporting Information.

$$C_{v,s}\frac{\partial T_s}{\partial t} = \frac{6h_s}{d_p}\left(T_g - T_s\right) + (-\Delta H)\frac{\partial \bar{q}}{\partial t} \tag{17}$$

$$\begin{aligned} &-\frac{\lambda_g}{C_{v,g}}\frac{\partial^2 T_g}{\partial z^2} + v\frac{\partial T_g}{\partial z} + \frac{\partial T_g}{\partial t} + \left(\frac{1-\varepsilon_b}{\varepsilon_b}\right)\left(\frac{C_{v,s}}{C_{v,g}}\right)\frac{\partial T_s}{\partial t} \\ &= \left(\frac{1-\varepsilon_b}{\varepsilon_b}\right)\left(\frac{-\Delta H}{C_{v,g}}\right)\frac{\partial \bar{q}}{\partial t} - \frac{4h_w}{\varepsilon_b d_p C_{v,g}}\left(T_g - T_w\right) \end{aligned} \tag{18}$$

$$\begin{aligned} &-\lambda_w\frac{\partial^2 T_w}{\partial z^2} + \rho_w C_{p_w}\frac{\partial T_w}{\partial t} - h_w\,\frac{4\,d_{b,in}}{d_{b,out}^2 - d_{b,in}^2}\left(T_g - T_w\right) + \\ &\frac{2/d_{b,in}}{\frac{\ln\left(d_{b,out}/d_{b,in}\right)}{\lambda_w} + \frac{2}{h_{amb}d_{b,out}}}\,\frac{4\,d_{b,out}^2}{d_{b,out}^2 - d_{b,in}^2}\left(T_w - T_{amb}\right) = 0 \end{aligned} \tag{19}$$

With $C_{v,s}$ the volumetric heat capacity of the solid, T_s the temperature of the solid phase, T_g the temperature of the gas phase, ΔH the heat of adsorption, λ_g the heat conductivity of the gas, $C_{v,g}$ the volumetric heat capacity of the gas, T_w the temperature of the walls, λ_w the heat conductivity of the

walls, ρ_w the density of the walls, $C_{p,w}$ the isobaric heat capacity of the walls, $d_{b,in}$ and $d_{b,out}$ the inner and outer diameter of the column, and T_{amb} the ambient temperature outside the adsorption bed.

Parameters determination was made by linking Aspen Adsorption and Matlab to use the surrogateopt function. This optimization method builds an approximate model based on a limited number of simulations and optimizes this model instead of the full Aspen model (Forrester et al., 2008). The objective function minimized the squared difference between experimental and modelled breakthrough curves by adjusting the parameters to be determined. From this methodology, linear driving force coefficient for CO_2 and N_2, gas-wall and outside heat transfer coefficients, bypass fraction (used in solid-gas heat transfer coefficient calculation developed in Supporting Information), bed tortuosity (used in gas dispersion coefficient), and heat capacity of the adsorbent were estimated to fit the experimental data.

2.2.3 Vacuum pressure swing adsorption cycles

The VPSA cycle described in Section 2.1.4 was implemented in Aspen Adsorption © V14 software using the same equations as in Section 2.2.2. The unibed approach was used for the interactions between the three adsorption beds, saving and replaying the flow rate, temperature, pressure, composition and enthalpy of the streams (Jiang et al., 2004). The cycles simulation was performed until the change in purity and recovery between two consecutive cycles was less than 0.1% (same stopping criteria as the experimental VPSA pilot (Henrotin et al., 2024)) assuming steady state is reached.

Two systems were investigated in this work. Firstly, the VPSA pilot was simulated under the same operating conditions as the experimental measurements to compare the results and validate the simulation for a 15/85 CO_2/N_2 mixture with a flow rate of 1 Nm^3/h. The parameters for this simulation are given in Table 1. The vacuum pump performance curve is used (Figure S~~2~~7 in Supporting Information) and allows to compute the pumping speed based on the inlet pressure. The decrease of pressure in the adsorption column was computed using the mass balance (equation 15). The isentropic efficiency of the compressors was set to 85%, while the vacuum pump isentropic efficiency was estimated using equation 20, which is dependent on the vacuum level, giving a more realistic estimation of energy consumption (Maruyama et al., 2020).

$$\eta = 0.8\frac{19.55p}{1+19.55p} \tag{20}$$

The second system simulated is an industrial VPSA pilot located at Technology Center Mongstad (TCM), operating with the same adsorbent material as the laboratory pilot under the MOF4AIR project. Based on the laboratory-scale results, the pilot was simulated with a similar flue gas stream coming from a residue fluid catalytic cracking (RFCC) unit. Three CO_2 concentrations were considered: 15% of CO_2, but also 10% and 5% CO_2 as these levels are representative of TCM's flue gas composition. The industrial pilot consists of three adsorption beds, each with a volume of 41 L, with a diameter of 0.3 m and a length of 0.58, operating the same VPSA cycle as the laboratory scale system. The vacuum pump performance curves of this pilot were also implemented in the simulation and are given in Supporting Information with Figure S16 for co-current evacuation and Figure S17 for counter-current evacuation. However, unlike the lab-scale setup, this equipment does not have pressure regulation. As for the laboratory scale, the full list of parameters used for the industrial simulation are also given in Table 1.

Table 1: Parameters used for the simulation of the laboratory and industrial VPSA pilot.

Parameter	Value for lab-scale pilot	Value for industrial pilot	Source
ε_{ads} [-]	0.35	0.35	Assumed

ρ_{ads} [kg.m^{-3}]	554.65	554.65	Derived from mass and geometry
ε_{bed} [-]	0.3	0.3	Derived from density of adsorbent and bed
ρ_{bed} [kg.m^{-3}]	385	385	Measured
d_p [m]	0.00247	0.00247	Measured
ϕ_{ads} [−]	0.83	0.83	Measured
L_{bed} [m]	0.3	0.58	Measured
$d_{bed,in}$ [m]	0.0701	0.3	Measured
$d_{bed,out}$ [m]	0.0761	0.306	Measured
Initial feed flow rate [Nm³/h]	1	30-100	VPSA pilot operating condition
Initial CO_2 fraction [%]	15	5-15	VPSA pilot operating condition
Feed temperature [°C]	20	30	VPSA pilot operating condition
Ambient temperature [°C]	20	30	VPSA pilot operating condition
M_{CO2} [g.mol^{-1}]	44	44	/
M_{N2} [g.mol^{-1}]	28	28	/
σ_{12} [Å]	3.8695	3.8695	(Poling et al., 2001)
ϵ_{12}/k [K]	118	118	(Poling et al., 2001)
k_{LDF} CO_2 [s^{-1}]	0.0542	0.0542	Fitted from breakthrough curves
k_{LDF} N_2 [s^{-1}]	6.4778	6.4778	Fitted from breakthrough curves
τ_b [-]	1.80	1.63	Fitted from breakthrough curves for lab scale and computed from $1/(0.45 + 0.55\varepsilon_b)$ for industrial scale
φ [−]	0.1040	0.014	Fitted from breakthrough curves for lab-scale and computed from 2 $d_p/d_{bed,in}$ for industrial scale
h_w [$W.m^{-2}.K^{-1}$]	4.19	Not constant, determined with equation S22 in Supporting Information	Fitted from breakthrough curves
h_{amb} [$W.m^{-2}.K^{-1}$]	4.29	Not constant, determined with equation S23 to S26 in Supporting Information	Fitted from breakthrough curves
ΔH_{CO2} [kJ.mol^{-1}]	-29.37	-29.37	Obtained from adsorption isotherms with Clausius-Clapeyron method
ΔH_{N2} [kJ.mol^{-1}]	-16.16	-16.16	Obtained from adsorption isotherms with Clausius-Clapeyron method
$C_{p,s}$ [J.kg^{-1}.K^{-1}]	1326	1326	Fitted from breakthrough curves
$C_{p,w}$ [J.kg^{-1}.K^{-1}]	500	500	Assumed
λ_s [W.m^{-1}.K^{-1}]	0.06	0.06	(Permyakova et al., 2017)
λ_w [W.m^{-1}.K^{-1}]	15	15	Assumed
ρ_w [kg.m^{-3}]	7990	7990	Assumed

2.3 Surrogate and optimization

The study and optimization of the cycle at both laboratory and industrial scales were conducted using the surrogate model. Surrogate modelling allows to reproduce the behavior of a time-consuming model with a simplified model, built using a limited number of simulations. For the laboratory scale, two surrogate models were compared: kriging model which assumes a spatial correlation between the outputs and inputs of the model (Forrester et al., 2008; Kudela & Matousek, 2022), and artificial neural network (ANN) which uses multiple layers of interconnected neurons using simple function between the inputs and the outputs (Du & Swamy, 2019; Kudela & Matousek, 2022). The kriging model used in this work is composed of a constant term and a stochastic term using correlation functions (kernels). Four kernels were compared: Radial basis function (RBF), rational quadratic (RQ), Matern 3/2, and Matern 5/2 (Kudela & Matousek, 2022; Rasmussen & Williams, 2005). For each kernel, the constant term and the hyperparameters were fitted using training data. More details about the kriging model

can be found in Section 6.1.1. of the Supporting Information. Feed forward network is used as ANN model to create a surrogate model since this network is able to represent numerous complex models, including VPSA (Du & Swamy, 2019; Streb & Mazzotti, 2022; Subraveti et al., 2019; Z. Wang et al., 2022). Different network architectures were investigated to find the optimal number of layers and neurons. One- and two-layers networks with 10, 20, 30 or 40 neurons per layer were trained for this work. For each architecture, the weights, biases, regularization terms, and activation functions were optimized using training data. More information on the ANN model can be found in Section–6.1.2. of the Supporting Information.

In practice, the surrogate models were implemented using the SciKit Learn library (Pedregosa et al., 2011) in Python, employing the "GaussianProcessRegressor" model for Kriging and "MLPRegressor" for ANN. Latin hyper cube sampling, combined with the Enhanced Stochastic Evolutionary algorithm (Jin et al., 2005), was used to generate a set of parameters which will be simulated in Aspen Adsorption. The results obtained from VPSA simulations were then used to construct the surrogate models. The data obtained were randomly divided into a training set (70%) and a validation set (30%). Before training, input and output data were scaled to have a mean equal to zero and a unit variance to improve the fitting procedure (Du & Swamy, 2019; Forrester et al., 2008; Rasmussen & Williams, 2005). Cross-validation with 10 folds is used during the training step to avoid overfitting and have a more robust model.

Surrogate models obtained can be used to study the effects of different variables on the VPSA unit or to find the optimal operating conditions with minimal computational resources. A multi-objective optimization was carried out using the Non-Dominated Sorting Genetic Algorithm II (NSGA-II) (Deb et al., 2002). Genetic algorithms have previously been used for the optimization of VPSA unit (Beck et al., 2015; Haghpanah et al., 2013; Khurana & Farooq, 2016b; Nguyen et al., 2023; Z. Wang et al., 2022) allowing to find the pareto between different variables (purity, recovery, productivity, and energy consumption). The Pymoo toolbox in Python (Blank & Deb, 2020) was used to implement NSGA-II by using the surrogate models built from Aspen Adsorption simulation results. NSGA-II was also directly applied with Aspen Adsorption to compare and validate the pareto obtained from the surrogate models.

For the lab-scale pilot, five variables were optimized for a unit treating a flow rate of 1 Nm^3/h containing a 15/85 CO_2/N_2 mixture: adsorption time [60-400 seconds], light reflux time [20-360 seconds], co-current evacuation time [20 – 40 seconds], co-current evacuation pressure [0.2 – 0.8 bar], light reflux flow rate [0.05 – 0.5 Nm^3/h]. Parameters studied and bounds are summarized in Table 2. These parameters are based on the experiments performed on a previous study where feed flow rate, feed concentration, adsorption pressure and counter-current evacuation are constant (Henrotin et al., 2024). The three times studied fully described the VPSA cycle used in this work and the bounds were determined with the limitation of the laboratory pilot (minimum 20 seconds per step), and the breakthrough curve experiments performed for the upper bound of adsorption time. In this work the upper bound was increased to 400 seconds to check if a higher adsorption time can increase the performance. Upper bound of light reflux time is determined by the upper bound of adsorption time with the equations (1) to (3). For co-current evacuation time, this step must be fast, and an upper bound of 40 seconds is kept as for the experimental work. Co-current evacuation pressure was studied between a slightly higher pressure than the counter-current evacuation pressure (0.2 bar) and below the atmospheric pressure (0.8 bar). Light reflux flow rate bounds are determined based on the physical limitations of the VPSA pilot as detailed in previous work (Henrotin et al., 2024). The adsorption pressure was set to 2 bar, and the counter-current evacuation pressure to 0.1 bar for all simulations (Henrotin et al., 2024).

Six variables were considered for the industrial case: the three times which defined the VPSA cycle as for the lab-scale unit (adsorption time [40 – 200 seconds], light reflux time [15 -160 seconds] and co-current evacuation time [5 – 25 seconds]), the feed flow rate [30 – 100 Nm^3/h] and the CO_2 concentration in the feed gas [5 – 15%] since the pilot will be used with various flue gas stream, the adsorption pressure [1.01 – 2 bar], and], the light reflux flow rate [0.1 – 20 Nm^3/h]. Parameters studied and bounds are also summarized in Table 2. Bounds for the time of the steps of the cycle are determined in a similar way to the laboratory pilot, with shorter adsorption time since the ratio between feed flow rate and volume is higher for the industrial pilot compared to the laboratory one. The minimum time for each step is also lower (5 seconds) based on the specification of the pilot. The range of feed flow rate and CO_2 concentration are based on the gas stream which will be tested at TCM test site and the limitations of the industrial pilot. Finally, adsorption pressure between atmospheric and 2 bar (same as the laboratory pilot) was studied. The pressure levels during the two evacuation steps were not directly controlled and are related to the evacuation time and the vacuum pump performance curves.

Table 2: Upper and lower bounds of the parameter tested by simulation for the experimental and industrial pilot.

Parameter	Lower bound laboratory	Upper bound laboratory	Lower bound industrial	Upper bound industrial
Adsorption time [s]	60	400	40	200
Light reflux time [s]	20	360	15	160
Co-current evacuation time [s]	20	40	5	25
Adsorption pressure [bar]	/	/	1.01	2
Co-current evacuation pressure [bar]	0.2	0.8	/	/
Feed flow rate [Nm^3/h]	/	/	30	100
Light reflux flow rate [Nm^3/h]	0.05	0.5	0.1	20
CO_2 feed concentration [%]	/	/	5	15

3 Results and discussion

3.1 Adsorption isotherms

Experimental adsorption isotherms obtained for CO_2 and N_2 on MIL-160(Al), and the corresponding model fits, are presented on Figure 2. In addition, the N_2 adsorption isotherms below 2 bar are represented in Figure S1 in Supporting Information. As observed, the Langmuir model is in good agreement with the experimental data, showing a R^2 of 99.07% for CO_2, and 99.89% for N_2. NRMSD values are also low, at 1.44% for CO_2 and 0.59% for N_2, indicating a strong predictive capability of the model.

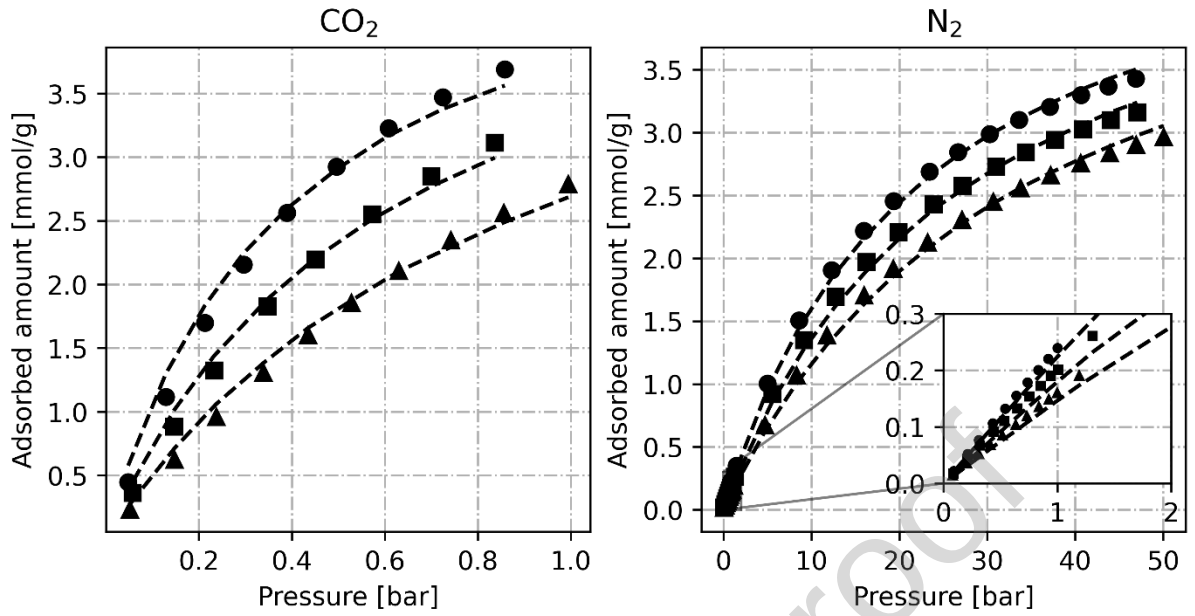

Figure 2: Experimental and fitted adsorption isotherms for CO_2 and N_2 on MIL-160(Al). Circle = 20°C experimental; square = 30°C experimental; triangle = 40°C experimental; dashed lines: Langmuir model.

The parameters obtained from the fitting of experimental data, along with their 95% confidence intervals, are given in Table 2: Langmuir model parameters obtained from experimental adsorption isotherms for CO_2 and N_2.for both CO_2 and N_2. The heat of adsorption, determined using the Clausius Clapeyron method at 0.1 mmol/g adsorbed, is -29.37 kJ/mol for CO_2 and -16.16 kJ/mol for nitrogen. More details on working capacity and selectivity can be found in previous work (Henrotin et al., 2024).

Table 3: Langmuir model parameters obtained from experimental adsorption isotherms for CO_2 and N_2.

	CO_2	N_2
q_s [mmol/g]	5.14 ± 0.14	5.14 ± 0.14
b_0 [1/bar]	$2.32 \times 10^{-6} \pm 1.80 \times 10^{-6}$	$3.93 \times 10^{-5} \pm 2.37 \times 10^{-5}$
ΔH [kJ/mol]	-34.01 ± 2.00	-17.21 ± 1.56

The comparison between the extended Langmuir model, and IAST for co-adsorption prediction was made by generating 10 000 points for different temperatures (-10 to 50°C), pressures (0.001 to 2 bar), and CO_2 concentrations (0 to 100%) with a latin-hypercube design (McKay et al., 1979), and computing the adsorbed amounts obtained with the two models. Figure S2 in the Supporting Information shows the predicted adsorbed amounts for extended Langmuir versus the adsorbed amounts predicted by IAST. As represented by the straight lines, results obtained with IAST and extended Langmuir are similar, giving a R^2 of 1 for both CO_2 and N_2 adsorbed amount. The mean absolute error between both models is 10^{-11} mmol/g, which is the numerical error made by the computer. Since IAST is based on implicit equations the extended Langmuir model will be used for simulating the VPSA process, as it significantly reduces computational expense while maintaining accuracy.

3.2 Breakthrough curves

Eleven breakthrough curve experiments have been carried out using the setup described in Section 2.1.3. Three different flow rates were tested: 0.3, 0.6 and 1 Nm³/h, in addition to different CO_2 concentrations. For all flow rates 10%, 15% and 30% were tested, while for 0.6 Nm³/h, additional concentrations of 20% and 50% were also investigated. Results obtained are given in Figure 3. As

observed, the breakthrough curves become sharper as the CO_2 concentration increases for a given flow rate. For a given CO_2 concentration, the curve profiles remain similar across different flow rates. Temperature profiles for the experiments performed with the column 1 containing an insertion sleeve (temperature probes located at 10 and 20 cm of the column inlet) are represented in Figure S3 to S6 in Supporting Information. The simulated temperature profiles are in relatively good accordance with the experiments showing a slight offset from the measurements.

The simulated breakthrough curves are also represented on Figure 3 by the solid lines. R^2 and NRMSD were computed over the same time scale as in Figure 3. Results are also given in Table S2 in the Supporting Information. The simulation gives a good overall representation of the data, giving a mean R^2 of 97.91% and a mean NRMSD of 4.34%. The main difference between the experimental and simulated data occurs towards the end of the rise of the breakthrough curve, where simulations predict a sharper curve, especially at higher CO_2 concentrations. This could be due to thermal effects which are not properly modelled, or gas channeling due to non-uniform adsorbent packing, leading to a lower packing density near the column walls which can occur even when the column to pellet diameter ratio is higher than 20 (Knox et al., 2016). From the optimization procedure, the linear driving force coefficients for CO_2 and N_2 were estimated to 0.054 and 6.478 1/s respectively, the gas to wall heat transfer coefficient is 4.19 W/(m².K), and wall to outside heat transfer coefficient is 4.29 W/(m².K). The bypass fraction determined is 0.1040, the adsorption bed tortuosity is 1.8, and the heat capacity is 1326 J/(kg.K). The value of k_{LDF} found for CO_2 is close to the value of 0.052 1/s found by Karimi et al., (2023) on the same material which seems to validate the results obtained. The value of k_{LDF} for N_2 is difficult to estimate by minimization, given its low impact on the process, and is probably overestimated, even if the nitrogen adsorption kinetic on MIL-160(Al) was reported to be fast (Karimi et al., 2023). The gas to wall heat transfer coefficient is lower than the prediction of the Yagi & Kunii, (1960) correlation (20 W/(m².K) for a flow rate of 1 Nm³/h), while the wall to outside heat transfer coefficient is close to the model with a wall emissivity of 0.4 – 0.5 (typical value for stainless steel (Hottel et al., 2007)). The bypass fraction from the gas-solid heat transfer coefficient is close to the value of $2\ d_p/d_b$ (0.07) suggested by Martin, (1978), and the bed tortuosity close to the value of $1/(0.45 + 0.55\varepsilon_b)$ (1.61) suggested by Ruthven, (1984). Lastly, the heat capacity obtained is higher than the previously reported value for powder (1117 J/(kg.K)) which could be due to the difference of sample and the binder used to shape the adsorbent (Permyakova et al., 2017).

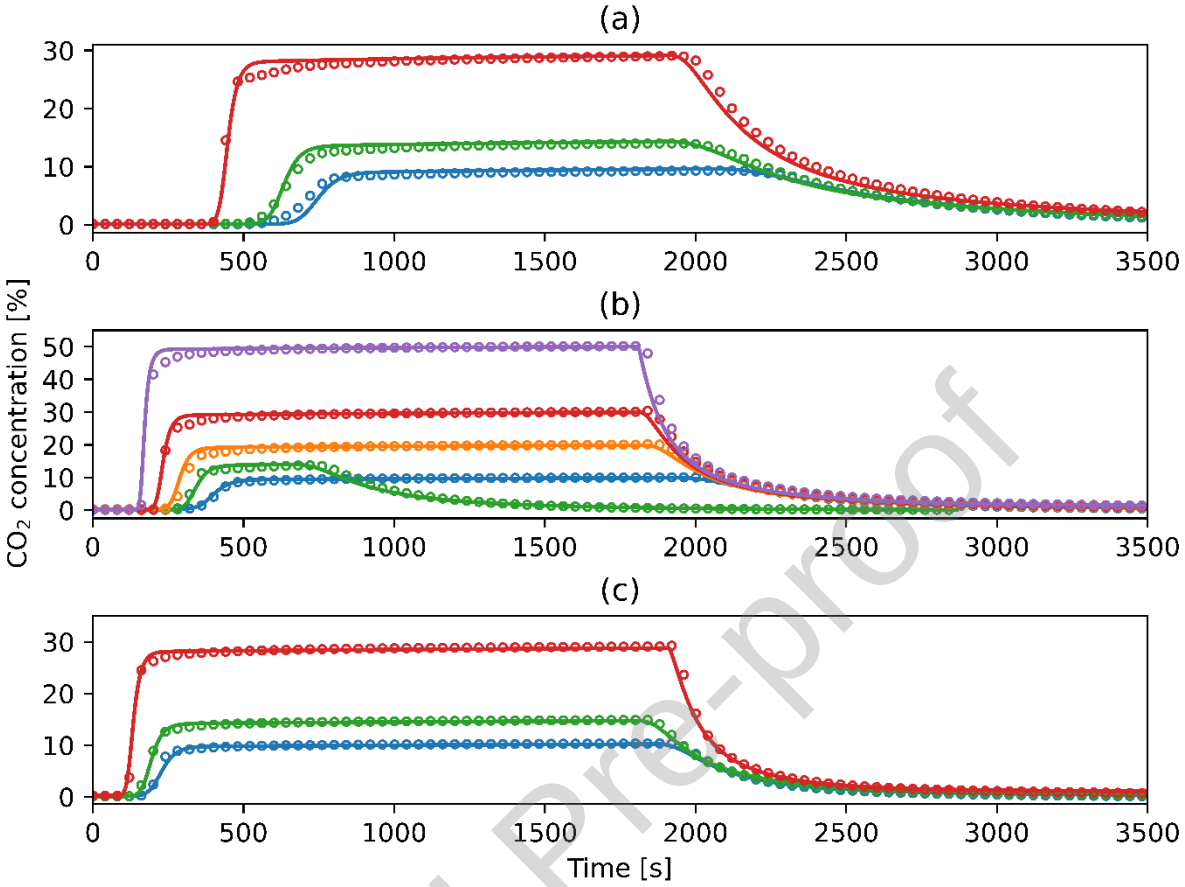

Figure 3: Breakthrough curves obtained (dots) and modelling in Aspen (lines) for 0.3Nm³.h⁻¹(a), 0.6Nm³.h⁻¹(b) and 1Nm³.h⁻¹(c) with different CO_2 concentrations (blue = 10%, green = 15%, orange = 20%, red = 30%, purple = 50%).

3.3 Laboratory scale vacuum pressure swing adsorption pilot

3.3.1 Simulation of experimental measurements

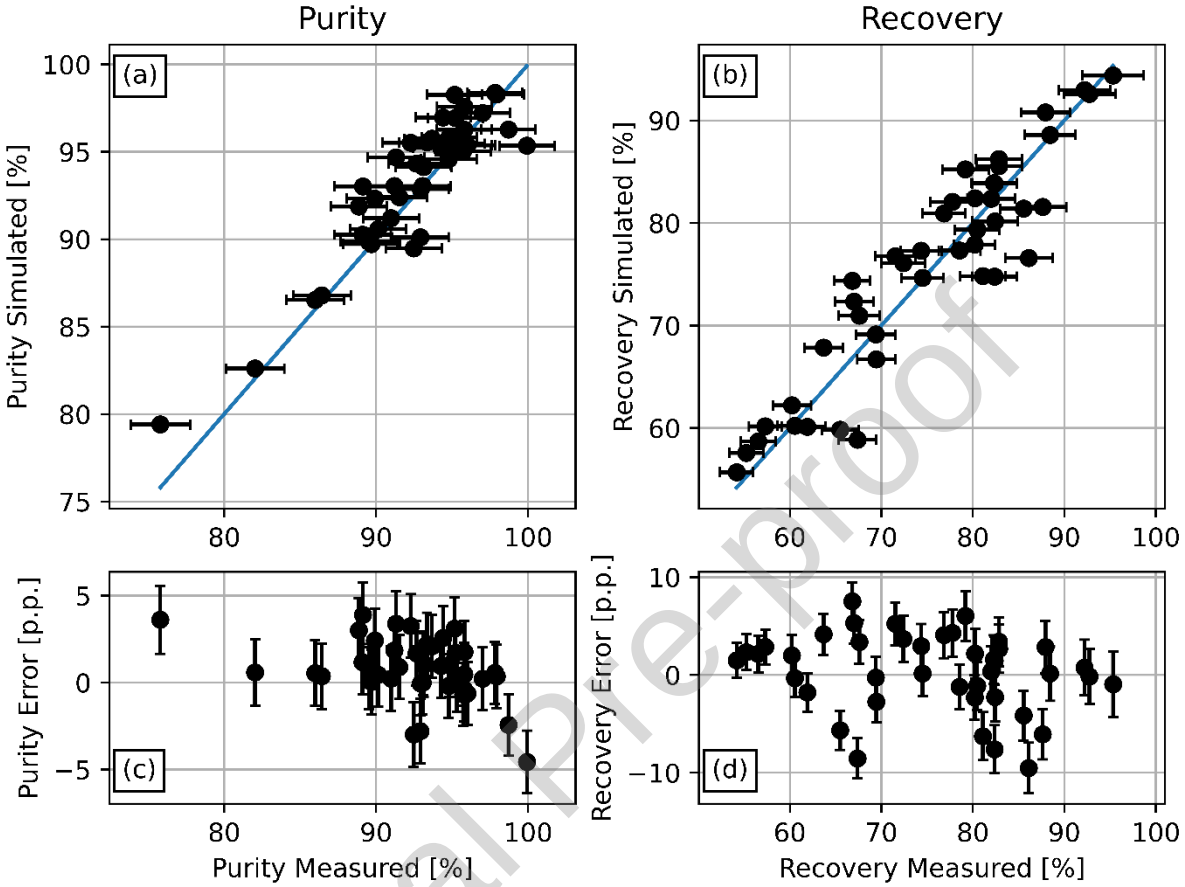

Figure 4: Purities and recoveries obtained by simulation versus experimental values. (a) Predicted vs actual value for purity, (b) predicted vs actual value for recovery, (c) error of the model (in percentage points) compared to purity measured, and (d) error of the model (in percentage points) compared to recovery measured.

The results of 42 experimental measurements and their corresponding simulations are represented in Figure 4 giving the simulated data versus the experimental data for purity (subplot(a)) and recovery (subplot (b)) and with the error (absolute difference between simulation and experimental given in percentage point) for purity (subplot (c)) and recovery (subplot(d)). Numerical values are also available in Table S3 in Section 5 of the Supporting Information. As observed, most measurements are well represented by the simulation giving a mean error of 1.47p.p. for purity and 3.19p.p. for recovery. For comparison, the mean experimental uncertainty is 1.84p.p.for purity and 2.36p.p. for recovery. Some measurements are less well predicted, leading to larger errors and reducing the value of R^2 and increasing NRMSD (see Table 3). The maximum error obtained is ± 4.57p.p. for purity and ± 9.53p.p. for recovery. Most of the purity errors (35 points over 42) are located between -3p.p. and +3p.p., and +5/-5p.p. for recovery (32 points over 42). Numerous factors can explain the discrepancies between simulation and experiment. The plug flow model used to simulate the adsorption bed does not account for radial effects such as gas channeling or heat gradient in radial direction. Other elements of the VPSA pilot such as dead space, valve, vacuum pump, … are probably not precisely modeled in the simulation model due to a lack of information from manufacturers.

However, the mean error in recovery and purity is similar to values reported in other simulations works as discussed in the introduction : Krishnamurthy et al., (2014) reported a mean normalized error for

purity and recovery of 2.3% and 2.55% respectively for the simulation of 8 experiments on a 2-bed 4-step pilot containing zeolite 13X. Estupiñan Perez et al., (2019) got a mean error of 1.67% and 1.42% for purity and recovery on four experiments performed on a lab-scale pilot with zeolite 13X. Nguyen et al., (2023) achieved a mean error for purity and recovery of 1.16% and 1.40% respectively for the simulation of eleven measurements for 2-bed 4-step pilot with CALF-20. Nevertheless, the number of works comparing simulation and VPSA pilot are quite limited in the literature. Moreover, the number of experimental measurements performed on VPSA installation is lower than the number of experiments performed in this work.

Table 4: Value of different indicators obtained for the representation of purity and recovery by the simulation.

	Purity	Recovery
Mean [p.p.]	1.47	3.19
Median [p.p.]	1.01	2.71
R^2 [%]	80.82	86.45
NRMSD [%]	7.97	9.69

In extent comparison between experiment and simulation was performed for experiment 4 which achieved an optimal balance between purity (90.1% ± 1.9%) and recovery (92.8% ± 2.8%). As shown in Figure 5, the simulated pressure during the counter-current evacuation and purge steps closely matches experimental data. NRMSD was computed for the tree profiles using equation (12) giving a deviation of 7.53% for the pressure and 9.86% for the flow rate and 8.19% for CO_2 concentrations. During co-current evacuation, the vacuum pressure sensor saturated at 1.1 bar explaining the constant value for 10 seconds. For the rest of this step, the simulated pressure profile is close to the experimental profile with small differences which are due to the pressure regulation in the VPSA pilot, which is difficult to reproduce by simulation. The same conclusion can be drawn for the flow rate profile. During counter-current evacuation and purge, the experimental and simulated profiles are close except during the transition between the two steps due to the opening and closing of the valves. For co-current evacuation, larger differences arise due to the pressure regulation. The CO_2 concentration profile predicted by the simulation matches experimental data, except after step transitions, which can be explained by pressure fluctuations in the gas analyzer due to valves operation, and the delay due to the distance between the vacuum pump outlet and the gas analyzer.

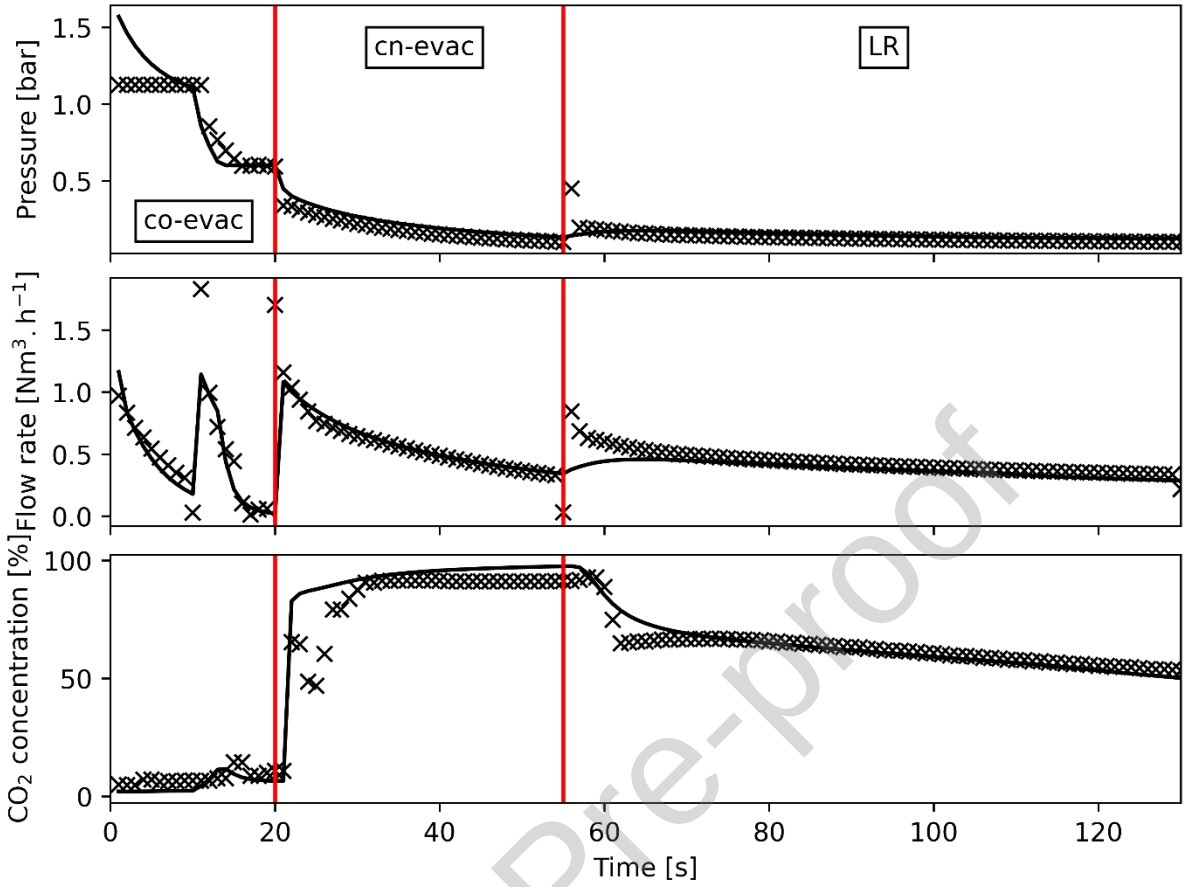

Figure 5: Comparison between pressure, flow rate and CO_2 concentration profile between experiment (cross marker) and simulation (line) during evacuation and purge for the experiment n° 4. Red lines are the transition between two steps.

The same observations and conclusions can be drawn for other parts of the VPSA pilot or other experimental measurements. VPSA pilot dynamics seem to be well represented by the simulation even if disturbing elements such as valve opening and closing, or co-current evacuation regulations are hard to model and are not perfectly described by the simulation model.

Moreover, the simulation model can be used to study the column behavior via adsorbed amount, gas phase concentration and temperature profiles in the column which are not directly measurable. Figure 6 presents these three profiles in the column over one cycle in steady-state conditions for experiment 4. In addition, evolution of adsorbed amount, gas phase concentration and temperature at three different positions in the bed are represented in Figure S9 to S11 in Supporting Information for clarity. As observed, the adsorbed amount for CO_2 is rapidly stable at the bottom of the adsorption bed during the adsorption step, meaning that the first layers of adsorbent are saturated (Figure 6a). From adsorption isotherm measurements, the adsorbed amount for a 15/85 CO_2/N_2 mixture at 2 bar and 20°C is equal to 2.29 mmol/g for CO_2 and 0.37 mmol/g for N_2 which are close to the values observed on Figure S9. For middle to the top of the column, the adsorbed amount of CO_2 continuously increases while the N_2 adsorbed amount decreases with the emergence of a saturation of adsorbed amount in the middle of the column. CO_2 gas phase concentration (Figure 6b) remains at 15% at the bottom of the bed and propagates during the adsorption step. Nevertheless, the CO_2 concentration at the end of the bed remains low (less than 1%) which allows to keep a high recovery. Temperature stays constant at the bottom of the bed (Figure 6c) and increases in the middle due to the adsorption of CO_2. During

heavy reflux step, the CO_2 quickly propagates in the columns by the flow coming from the column in light reflux step (67% CO_2, 2 bar, 20°C) as represented by Figure 6a and b. The adsorbed CO_2 amount has a sharp increase at the bottom of the column, and at the middle with a delay. This is due to the absence of plateau in the CO_2 adsorption isotherm of MIL-160(Al) in the relevant range of CO_2 partial pressures (Figure 2) that enables higher adsorbed quantities at higher partial pressures. Temperature increases in the bottom half of the column due to the adsorption (Figure 6c). The amount of adsorbed nitrogen decreases during this step. A displacement of the CO_2 adsorbed amount occurred during the co-current evacuation step, with a decrease at the bottom, and an increase at the middle and top of the column. CO_2 gas phase concentration is also shifted to the top of the column with a sharp increase in the middle of the column (40 to 80%) but remains low at the outlet with concentration of 12% at the end of this step. During this step, the N_2 adsorbed amount decreases sharply to reach almost 0 mmol/g at the bottom to the middle of the column. There is some nitrogen remaining at the top of the column. Temperature profile follows the same trend as gas phase concentration with the hot spot being displaced to the center of the bed. During counter-current evacuation and light reflux, the amount of CO_2 adsorbed in the column decreases with sharper variation at the middle and bottom. The effect of light reflux is more pronounced at the top of the column showing the importance of this step to reduce the adsorbed amount at this location. CO_2 gas phase concentration increases during the co-current evacuation step due to the desorption with concentration being close to 100% in the bottom of the bed at the end of the step. The concentration remains low at the top of the bed (20%) due to the low adsorbed amount in this part of the bed. Temperatures decrease in the bottom of the bed due to the strong desorption but remain high in the top of the bed. During light reflux, the CO_2 gas phase concentration drops due to the flow of nitrogen reach stream. A concentration of 50% of CO_2 remains in the bottom of the bed at the end of this step. Temperatures decrease in the whole bed due to the desorption and heat transfer with the gas. Finally, the adsorbed amount of N_2 increases as pressure rises during the light product pressurization step while the amount of adsorbed CO_2 remains constant. CO_2 gas phase concentration sharply drops with the adsorption and temperatures increase due to the compression of the gas from 0.1 to 2 bar. The 3D representation of adsorbed amount for CO_2 and N_2 are presented in Figure S8 in the Supporting Information.

On Figure 6a, we can observe that the top of the column keeps a low CO_2 adsorbed amount during the whole cycle compared to the rest of the column despite the displacement of CO_2 caused by heavy reflux and co-current evacuation, giving a good recovery. In addition, the adsorbed amount of nitrogen is very low at the start of the counter-current evacuation giving good purity. Optimization of the various cycle parameters is important in order to achieve an identical concentration profile for good CO_2 recovery and purity.

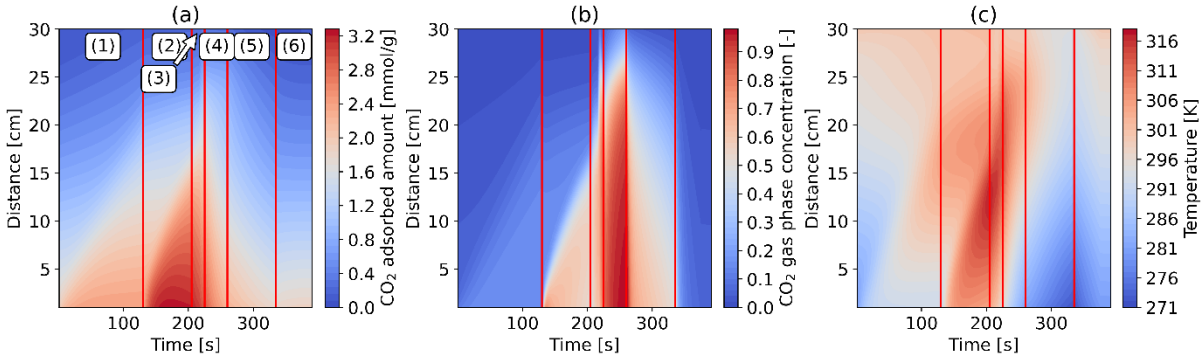

Figure 6: CO_2 adsorbed amount (a), CO_2 gas phase concentration (b) and temperature (c) profiles in the column for experiment n°4 during one cycle in steady state. Red lines are the transition between two steps. The steps are numbered in subfigure (a): (1) Adsorption, (2) heavy reflux, (3) co-current evacuation, (4) counter-current evacuation, (5) light reflux, (6) light product pressurization.

3.3.2 Optimization

The optimization procedure described in section 2.3 was applied to the lab-scale VPSA pilot model in Aspen Adsorption to find the pareto plot of purity and recovery. A first optimization was performed using NSGA-II algorithm on the Aspen model by linking the software to the optimization algorithm with a python script to find the pareto between purity and recovery. A population size of 50 was chosen for the optimization, and 150 generations were performed giving a total of 7500 simulations to generate the pareto plot. On the other hand, 1400 simulations were performed to train the two surrogate models, and 600 additional simulations were used to validate the trained models. The same training and validation datasets were used for both models.

Four kernels were compared for the surrogate model, and 14 network topologies were investigated for the artificial neural network model. Figure S12 gives the MSE and R^2 values obtained for kriging, and the same results for the topologies of the ANN are given in Figure S14 in the Supporting Information. The best-performing kernel was the Matern 5/2 with a R^2 of 99.77% and 99.69% and NRMSD of 1.14 10^{-2} and 9.2 10^{-3} for recovery and purity respectively. RBF and Matern 3/2 kernels gave close results with R^2 higher than 99% and NRMSD lower than 0.02. The ANN topology is more impacting than the kernel choice as represented by Figure S14 in Supporting Information. For a one-layer topology, increasing the number of neurons from 10 to 40 improved the accuracy of both recovery and purity. When adding a second layer, the best results were generally obtained when the size of the second layer is smaller than the first one. The (40,30) topology gave the best NRMSD value for recovery (8.1 10^{-3}), while the (40,20) topology was the best for purity (NRMSD equal to 6.2 10^{-3} for purity but 9.2 10^{-3} for recovery). ANN outperformed kriging in terms of R^2 and NRMSD for the validation set. Nevertheless, the R^2 is very high for both models (>99%) and NRMSD is relatively low (< 0.02).

The evolution of NRMSD and R^2 with the number of training points was studied for the Matern 5/2 kernel (Figure S13) and the (40,30) topology (Figure S15 in the Supporting Information). For the kriging model, NRMSD and R^2 trends suggest that additional simulations could improve accuracy, but the slope of the MSE curve seems to indicate that numerous simulations would be required to reach the same value of NRMSD as ANN model. For ANN, the slope of NRMSD seems stabilized at 1000 training points meaning that the model cannot be improved significantly by more simulations.

The surrogate models were then used to find the pareto front using NSGA-II. Figure 7 gives the graphical comparison between the purity-recovery pareto obtained with Aspen and with the kriging and ANN models. As observed, the ANN pareto front closely matches the one obtained from direct optimization of the Aspen model with small differences between the two curves. The optimization using the kriging model is less accurate with an overprediction of 4-5% of purity and recovery. Compared to the differences between simulation and the experimental results, the differences between the ANN model and the direct Aspen optimization are negligible. The pareto obtained shows that achieving both 95% of recovery and purity cannot be obtained under the investigated experimental conditions (1 Nm^3/h feed gas with 15% CO_2, adsorption pressure set to 2 bar, and an evacuation pressure of 0.1 bar). Nevertheless, for a recovery of 90%, the corresponding purity is 94% (with the ANN pareto). At a higher recovery of 95%, almost 90% of purity can be obtained. The performance of the pilot obtained by simulation is promising and close to the targets of a CO_2 capture process. Experimental results are also close to the pareto determined with experimental recovery/purity couple of (92.8%/90.1%) and (87.6%/96.0%) indicating that the experimental design carried out enabled us to find near-optimum conditions for the pilot.

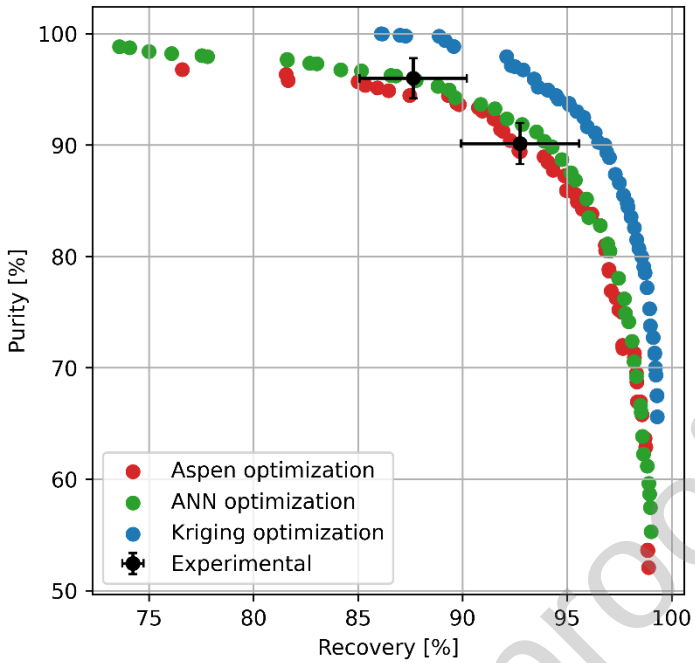

Figure 7: Comparison of pareto obtained with direct optimization of the Aspen model, and optimization of the surrogate models. Experimental recovery/purity couples (92.8%/90.1%) and (87.6%/96.0%) are also represented.

The parameters giving the pareto plot obtained with Aspen are represented on Figure 8 with the red line representing the point with 95% purity, and the blue line the point with 95% recovery. Adsorption times are mainly comprised between 125 and 175 s, and light reflux times are in the range 60-120 s. Co-current evacuation times are in the narrow range of 20-26 s, except for some points with very high purity where this step lasts 40-45 s. It seems that minimizing this step duration enhances both recovery and purity. Co-current evacuation pressures range between 0.46 and 0.65 bar, except at very high recoveries, which require a pressure of 0.79 bar. Light reflux flow rates are comprised between 0.05 and 0.18 Nm^3/h. From Figure 8, the best purities are obtained with longer adsorption and light reflux times, lower co-current evacuation pressures, and lower light reflux flow rates. On the other hand, best recoveries are obtained with higher light reflux flow rates, lower light reflux times, and higher co-current evacuation pressures. The two highlighted points in Figure 8 correspond to different conditions, with adsorption time of 147 s, light reflux time of 79 s, co-current evacuation time of 23 s and pressure of 0.65 bar, and a light reflux flow rate of 0.17 Nm^3/h for the recovery of 95% while the purity of 95% has an adsorption time of 175 s, light reflux time of 96 s, co-current evacuation time of 23 s and pressure of 0.52 bar, and light reflux flow rate of 0.12 Nm^3/h.

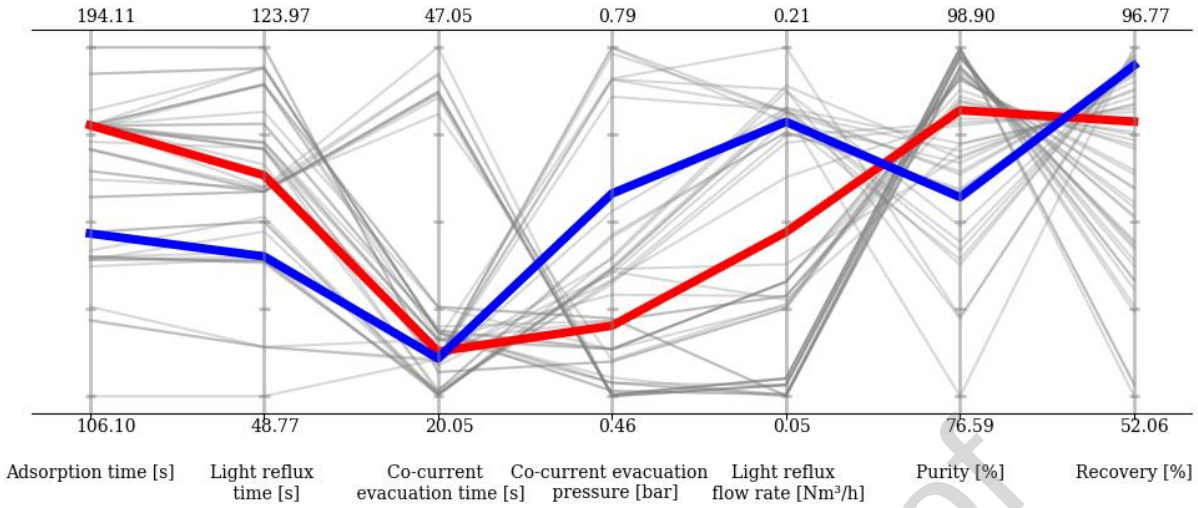

Figure 8: Coordinate plot obtained for the pareto plot. Red line: best point for a purity of 95%, blue line: best point for a recovery of 95%.

3.4 Industrial scale vacuum pressure swing adsorption pilot

The industrial pilot described in 2.2.3 was simulated using parameters obtained from the breakthrough curve simulation (Section 2.2.2), the size of the industrial columns, and the vacuum pump performance of the industrial pilot. Heat transfer coefficients between the gas and the inlet column wall are different from the lab-scale pilot ones and were computed using the equation described in Section 2.4. of the Supporting information. Coefficient between the outlet wall of the column and the ambient environment was calculated using the equations of Section 1.5. The complete list of simulation parameters is given in Table 1 in Section 2.2.3. 3000 simulations were performed within the bounds specified in Section 2.3 to find the optimal operating conditions for the industrial pilot. An artificial neural network was used as a surrogate model since this model performed better in lab-scale simulations. The same strategy as the lab-scale pilot was used, 70% of the simulations were used to train the surrogate model for purity, recovery, and energy consumption, while the remaining 30% were used for validation. Productivity was not determined with the ANN model since this indicator can be derived from feed flow rate, CO_2 concentration at the inlet, and recovery. Calculation procedure is given in Section 7.1. of Supporting Information. Different network topologies were studied to find the optimal configuration. Networks with one or two layers, containing 10, 20, 30, 40 or 50 neurons, were investigated. The accuracy of the surrogate model compared to validation points was evaluated using R^2 and NRMSD given in Figure S18 in the Supporting information. The best topology is not identical between purity, recovery and energy consumption: (50,40) network gives the lowest NRMSD for purity, the (50,30) network performed best for recovery, and the (40,40) network for energy consumption. The most suitable network for each indicator was used for the respective optimization of the industrial unit.

Four indicators are given in Table 4. The model obtained give a good representation of the validation points, with R^2 higher than 99%, and NRMSD lower than 1% for all three outputs. The mean absolute error (MAE) and median absolute error (MedAE) are both lower than 0.5% for purity and recovery which is well below the typical experimental error of a VPSA. The mean error in energy consumption is also low compared to the range of 250 to 2000 kWh/t_{CO2} obtained in the 3000 simulations of the industrial VPSA pilot.

Table 5: Value of different indicators obtained for surrogate model of the industrial pilot against the validation points for recovery, purity and energy consumption.

	Purity [%]	Recovery [%]	Energy [kWh/t_{CO2}]
R^2 [%]	99.79	99.92	99.93
NRMSD [%]	0.48	0.60	0.38
MAE	0.10	0.34	5.26
MedAE	0.05	0.24	3.54

The effect of CO_2 inlet concentration, feed flow rate, and adsorption pressure on the purity/recovery pareto of the industrial pilot was studied using the surrogate model. Figure 9 gives the pareto front obtained with four feed flow rates: 40, 60, 80 and 100 Nm³/h. For each flow rate, three CO_2 inlet concentrations were investigated as represented by the light, normal and dark colors. Blue points were obtained for atmospheric pressure during the adsorption step, while red points indicate a pressure of 2 bar. As observed, the CO_2 concentration in the feed has a low impact on the pareto front for a given flow rate and adsorption pressure. The 5% concentration can give slightly higher recovery compared to 10% and 15% at low feed flow rate, but the effect is negligible. As the feed flow rate increases, the pareto fronts shift to lower recovery, especially atmospheric adsorption pressure. At this pressure, the VPSA pilot is able to reach 90% recovery for 95% purity with a feed flow rate of 40 Nm³/h. Compared to the lab-scale pilot, the industrial pilot's vacuum pump reaches a vacuum level lower than 0.1 bar during counter-current evacuation, which can explain the improved results. At 100 Nm³/h, the maximum recovery for 95% purity is only around 55% for the three inlet CO_2 concentrations. Increasing the adsorption pressure to 2 bar gives a beneficial effect on the pareto of the industrial pilot, shifting the curves toward higher recoveries (red dots). With this higher adsorption pressure, the target of 95% purity and recovery can be obtained for a feed flow rate slightly below 60 Nm³/h for the three CO_2 concentrations. In addition, pair plot of purity, recovery, energy consumption and productivity is represented in Figure S20 in Supporting Information. This figure shows the beneficial effects of recovery on productivity and energy consumption. Nevertheless, high recoveries lead to low purity as represented in the pareto plots of Figure 9. Energy consumption and productivity remain constant for purity, lower than 90%. At higher purities, energy consumption rises sharply and productivity drops.

Distribution of decision variables of the optimization (adsorption time, light reflux time, co-current evacuation time and light reflux flow rate) related to the change of feed concentration or flow rate and adsorption pressure is represented in Figure S21 in supporting information. The optimum times of the cycle are dependent on the CO_2 concentration with a decrease of three times when the CO_2 concentration in the feed is increased. The higher amount of CO_2 in the flue gas leads to shorter cycle time to avoid the breakthrough of the column during the adsorption step. Co-current evacuation time is the most impacted by the change of CO_2 concentration with very short step time for 15% of CO_2. The adsorption column is probably more saturated, and a shorter step is required to avoid losing CO_2 during co-current evacuation. Light reflux flow rate is less impacted by the change of CO_2 concentration with value between 5 and 10 Nm³/h. Increase of feed flow rate leads to shorter cycle times as represented by adsorption and light reflux times but has no major effect on co-current evacuation time nor light reflux flow rate. Higher adsorption pressure slightly shifts the distribution of adsorption time with higher time possible at 2 bar compared to atmospheric pressure. The same behavior is observed for light reflux flow rate.

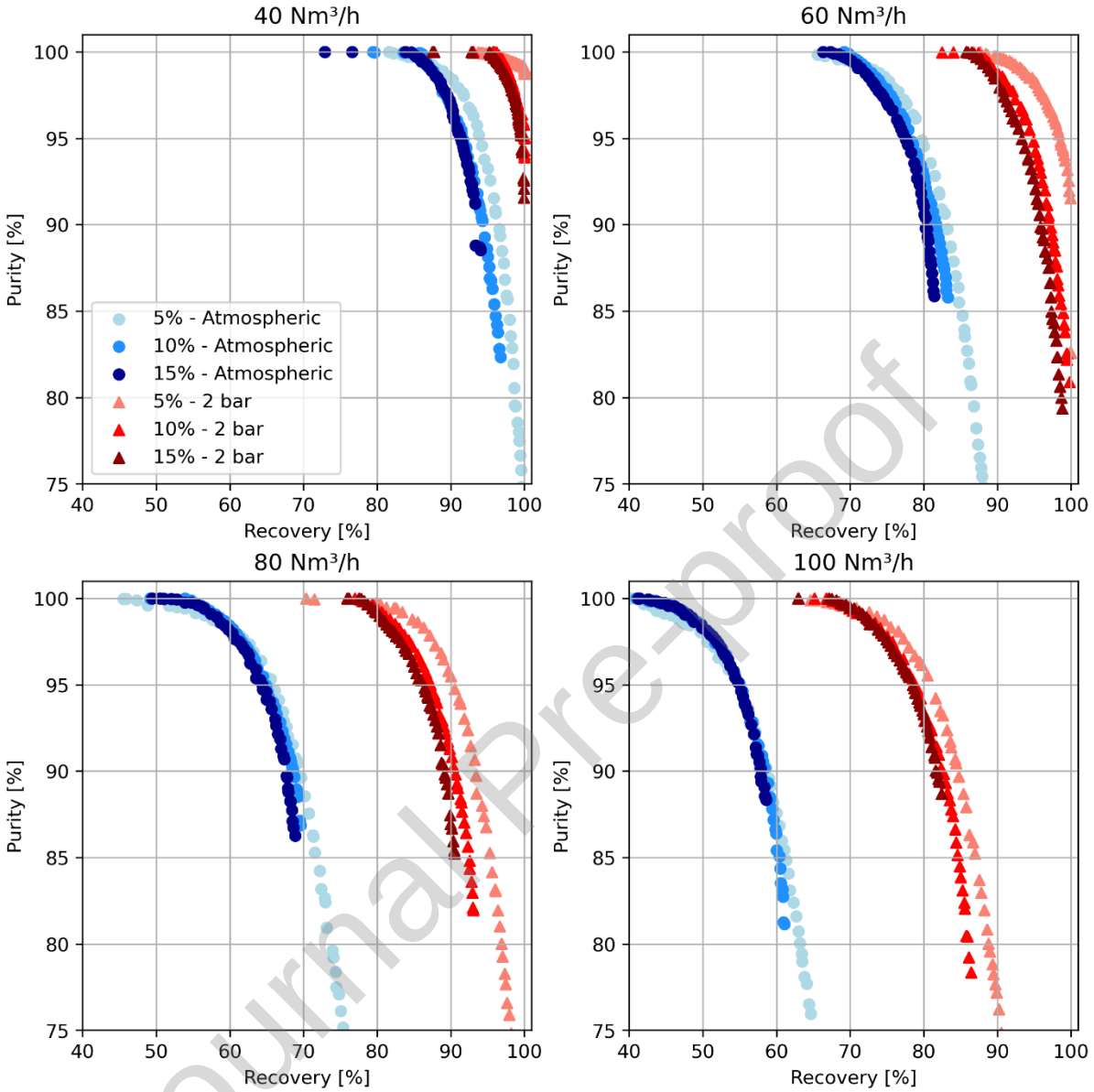

Figure 9: Purity-recovery pareto for different feed flow rates, inlet CO_2 concentrations and adsorption pressures on the industrial pilot. Light blue: 5% CO_2 at atmospheric pressure, blue: 10% CO_2 at atmospheric pressure, dark blue: 15% CO_2 at atmospheric pressure, light red: 5% CO_2 at 2 bar, red: 10% CO_2 at 2 bar, dark red: 15% CO_2 at 2 bar.

Since the targets of 95% purity and recovery can be obtained with the industrial pilot, the energy consumption and productivity of the VPSA unit were evaluated for the three CO_2 concentrations. The same optimization procedure as for the recovery-purity pareto using NSGA-II was applied to find the pareto of productivity and energy consumption with a constraint of at least 95% purity and recovery. The optimization procedure was performed at adsorption pressures of 1.01 and 2 bar to study the impact of pressure on pilot performance. Results of the optimization are given in Table 5. In addition, the profiles obtained in steady state for CO_2 adsorbed amount CO_2 gas phase concentration, temperature and pressure are represented in Figure S22 to S27

for the six optima of the Table 5. For atmospheric pressure, the optimal adsorption time decreases with increasing CO_2 concentration, ranging from 105 seconds for 5% CO_2 to 73 seconds for 15%. Light reflux time and co-current evacuation times follow the same trend with light reflux time between 38

and 74 seconds, and co-current evacuation time between 7 and 11 seconds. Light reflux flow rate also decreases as the inlet CO_2 concentration increases with a flow of 8.20 Nm^3/h for 5% CO_2 to 5.39 Nm^3/h for 15%. The feed flow rate which can be treated to reach 95% purity and recovery with an atmospheric adsorption pressure is quite low with only 30.92 to 37.06 Nm^3/h. This leads to low productivity (0.67 $t_{CO2}/(m^3_{ads}.day)$ for 5% CO_2 to 1.69 for 15%). The low feed flow rate also impacts energy consumption leading to high values especially for 5% CO_2 in the inlet (up to 1432 kWh/t_{CO2} at the lowest adsorption pressure).

Increasing the adsorption pressure up to 2 bar improves productivity by 70-80% but also surprisingly decreases energy consumption by 20%. This can be explained by the optimized feed flow rate, which is almost twice compared to the atmospheric pressure case, increasing the amount of CO_2 captured and thus increasing the denominator of the energy consumption, even if the numerator is larger due to the compression of the feed flue gas. Optimal operating conditions at 2 bar follow the same trends as at atmospheric pressure, where the adsorption and light reflux times are lower for higher CO_2 concentrations. Co-current evacuation time and light reflux flow rate also follow the same trends as the atmospheric pressure case, with a slightly higher flow rate for the light reflux.

The comparison between Figure 6 (laboratory pilot with 15% CO_2 in the flue gas and adsorption pressure of 2 bar) and Figure S27 (industrial pilot with the same flue gas concentration and adsorption pressure) reveals a lower CO_2 loading in the first layers of the bed at the beginning of the cycle for the industrial pilot compared to the laboratory one. During adsorption, CO_2 reaches the middle of the column with the laboratory setup while only a third of the industrial column is filled. Heavy reflux is less significant in the industrial pilot with CO_2 being adsorbed in the first layers of the column. Although the CO_2 fraction in the gas at the inlet seems similar on industrial and laboratory pilot as represented by subplots (b). CO_2 adsorbed amount decreases sharply to a low level during the evacuation steps which is probably due to the vacuum pump used in the industrial pilot being able to reach faster a lower level of vacuum as represented by the characteristics curve in Figure S17 and the vacuum level in subplot (d) of Figure S22. Temperature profiles look similar between industrial and laboratory pilot, except for the hot spot observed during heavy reflux for the laboratory scaler.

Results obtained by simulation assume a dry gas at the inlet of the VPSA unit. In real process application, the flue gas is generally saturated with water vapor. MIL-160(Al) studied in this work has an important affinity with water exhibiting high water capacity (>15 mmol/g for RH=20% at 30°C) and high heat of adsorption (-54 kJ/mol) (Cadiau et al., 2015; Silva et al., 2021). Interactions between CO_2 and H_2O reduce the CO_2 capacity of the adsorbent for RH higher than 5% and thus the global performance of the adsorption unit. The presence of water must be considered in the whole treatment of the flue gas by including the additional energy consumption of a dryer unit such as TSA unit using silica gel.

Energy consumption obtained by simulation is close to values obtained with industrial adsorption pilot in literature: Krishnamurthy et al., (2014) obtained a productivity comprised between 0.87 and 1.4 $t_{CO2}/(m^3_{ads}.day)$ and an energy consumption comprised between 339 and 582 kWh/t_{CO2} with 2-bed 4-step pilot containing zeolite 13X and treating a flue gas of 56.9 Nm^3/h with 15% CO_2. It should be noted that this pilot operates with regeneration time higher than adsorption leading to non-continuous treatment of the gas. CALF-20 tested in the same cycle at laboratory scale yield a productivity 0.49-1.14 $tCO_2/(m^3ads.day)$ and 140-192 kWh/t_{CO2} (Nguyen et al., 2023). Liu et al., (2012) studied a 3-bed 8-step pilot wit zeolite 13X and obtained 0.52-0.84 $t_{CO2}/(m^3_{ads}.day)$ as productivity and 497-867 kWh/t_{CO2}. Compared with the simulation made by Khurana & Farooq, (2016b) on the same cycle, the energy consumption obtained in this work is almost two times higher from the values obtained in their work with UTSA-16 (125 kWh/t_{CO2} for minimum energy consumption and 289 kWh/t_{CO2} for maximum

productivity). They also obtained very high productivity (8-18 $t_{CO2}/(m^3_{ads}.day)$) with UTSA-16 compared to the pilot in this work. This difference could be explained by the fact that the industrial pilot of this work is not able to regulate pressure, giving a lesser degree of freedom for optimization. Moreover, in the work of Khurana & Farooq, (2016b), some evacuation steps are very short (15 seconds to reach 0.02 atm) which is not possible with the pilot of this work. The 3-bed 6-step cycle studied in this work is also able to compete with in two-stage VPSA units described in the literature. Shen et al., (2012) studied experimentally and by simulation a two-stage unit of 2-bed 4-step VPSA using activated carbon to treat a flue gas containing 15% of CO_2. This unit is able to reach high purity (>95%) but with a maximum recovery of 82.86%. Energy consumption obtained for this unit are lower than this work with 250.67 kWh/t_{CO2}. Productivity is also lower with 0.67 $t_{CO2}/(m^3_{ads}.day)$. The same research group studied an alternative configuration with a 3-bed 5-step cycle for the first stage and a 2-bed 5-stpe cycle for the second stage using zeolite 13X for both stages. This unit was able to reach high purity (94.35%) and high recovery (95.64%) with a very low energy consumption (159.4 kWh/t_{CO2}), but with a productivity almost six time lower than this work (0.52 $t_{CO2}/(m^3_{ads}.day)$) (L. Wang et al., 2012). More recently X. Yu et al., (2022) studied experimentally a two-stage 2-bed 4-step VPSA using activated carbon in the first unit and zeolite 13X in the second. They were able to reach purity and recovery close to 95% with an energy consumption of 291 kWh/t_{CO2} and a productivity of approximately 1.37 $t_{CO2}/(m^3_{ads}.day)$ for a flue gas of 15% CO_2. Dual reflux PSA is a particular configuration of two-bed cycles where feed gas is injected at the middle of the column and reflux are performed simultaneously with the adsorption step. This configuration has been studied by Li et al., (2016) showing impressive results with 99.18% of purity and 99.62% of recovery for an energy consumption of 538 kWh/t_{CO2} to treat a flue gas containing 15% of CO_2.

Table 6: Optimum found for a purity and recovery of at least 95% with different CO_2 concentrations in the feed and different adsorption pressures.

Case	5% CO_2 p_{atm}	10% CO_2 p_{atm}	15% CO_2 p_{atm}	5% CO_2 2 bar	10% CO_2 2 bar	15% CO_2 2 bar
Adsorption time [s]	105	97	73	93	69	63
Light reflux time [s]	74	63	38	58	33	25
Co-current evacuation time [s]	11	8	7	11	9	8
Feed flow rate [Nm^3/h]	37.06	33.30	30.92	68.87	59.03	55.62
Light reflux flow rate [Nm^3/h]	8.20	6.19	5.39	10.30	7.73	6.26
Purity [%]	95.00	95.00	95.00	95.01	95.01	95.07
Recovery [%]	95.11	95.09	95.06	95.01	95.00	95.03
Productivity [$t_{CO2}/(m^3_{ads}.day)$]	0.67	1.21	1.69	1.25	2.15	3.04
Energy consumption [kWh/t_{CO2}]	1432	784	531	1087	579	405

4 Conclusion

A unibed simulation model for the 3-bed 6-step cycle in Aspen Adsorption software was developed in this work, including interactions between process steps and the actual behavior of the vacuum pump for enhanced accuracy. The pure adsorption isotherms on MIL-160(Al) were measured and adsorption parameters were determined by fitting the Langmuir model. The column model including mass, momentum, and energy balances, was then used to fit breakthrough curve experiments performed on

a lab-scale VPSA pilot. Kinetic parameters, heat capacity, and heat transfer parameters were obtained from this procedure, giving an overall good fitting with a mean R^2 of 97.91% between experimental data and breakthrough curve simulations. All the parameters obtained were used to simulate a laboratory VPSA pilot performing the 3-bed 6-step cycle with a feed flow rate of 1 Nm^3/h containing a 15/85 CO_2/N_2 mixture. 42 experimental measurements were compared with the simulation model, giving a mean absolute error on purity and recovery of 1.47% and 3.19% respectively. The comparison was further extended by analyzing pressure, flow, and composition profiles, showing a good agreement between model prediction and experimental measurements.

Optimization of the VPSA model for laboratory scale was performed using the NSGA-II both directly within Aspen Adsorption and via a surrogate model. A comparison between direct optimization, kriging, and artificial neural networks revealed that ANN performs better for the representation of the complete simulation model, especially when computing the pareto front. The study of different topologies was important in minimizing differences between ANN and the complete simulation model.

Finally, the validated model was used to simulate an industrial VPSA pilot to be operated within the MOF4AIR project. A surrogate model using ANN was used to compute the pareto front for different feed flow rates, CO_2 concentrations, and adsorption pressures. Feed flow rate and adsorption pressure play an important role in the pareto front. Optimization of energy consumption and productivity for purity and recovery higher than 95% resulted in an energy consumption of 413.19 kWh/t_{CO2} and a productivity of 3.03 $t_{CO2}/(m^3_{ads}.day)$ for a flue gas composition of 15% CO_2.

Declaration of interests

The authors declare that they have no known competing financial interests or personal relationships that could have appeared to influence the work reported in this paper.

Acknowledgements

This project has received funding from the European Union's Horizon 2020 research and innovation program under grant agreement No. 831975. This output reflects only the author's view and the European Union cannot be held responsible for any use that may be made of the information contained therein.

CRediT authorship contribution statement

A. Henrotin: Writing – review & editing, Writing – original draft, Visualization, Validation, Methodology, Investigation, Formal analysis, Data curation, Conceptualization. **N. Heymans:** Writing – review & editing, Writing – original draft, Validation, Supervision, Methodology, Investigation, Data curation, Conceptualization. **M.-E. Duprez:** Writing – review & editing, Project administration. **G. De Weireld:** Writing – review & editing, Validation, Supervision, Project administration, Funding acquisition, Conceptualization.

Alkebsi, K., & Du, W. (2021). Surrogate-assisted multi-objective particle swarm optimization for the operation of CO2 capture using VPSA. *Energy*, *224*, 120078. https://doi.org/10.1016/j.energy.2021.120078

Bahamon, D., Díaz-Márquez, A., Gamallo, P., & Vega, L. F. (2018). Energetic evaluation of swing adsorption processes for CO2 capture in selected MOFs and zeolites: Effect of impurities. *Chemical Engineering Journal*, *342*, 458–473. https://doi.org/10.1016/J.CEJ.2018.02.094

Bains, P., Psarras, P., & Wilcox, J. (2017). CO2 capture from the industry sector. *Progress in Energy and Combustion Science*, *63*, 146–172. https://doi.org/10.1016/j.pecs.2017.07.001

Beck, J., Friedrich, D., Brandani, S., & Fraga, E. S. (2015). Multi-objective optimisation using surrogate models for the design of VPSA systems. *Computers and Chemical Engineering*, *82*, 318–329. https://doi.org/10.1016/j.compchemeng.2015.07.009

Billemont, P., Heymans, N., Normand, P., & De Weireld, G. (2017). IAST predictions vs co-adsorption measurements for CO2 capture and separation on MIL-100 (Fe). *Adsorption*, *23*(2–3), 225–237. https://doi.org/10.1007/s10450-016-9825-6

Blank, J., & Deb, K. (2020). Pymoo: Multi-Objective Optimization in Python. *IEEE Access*, *8*, 89497–89509. https://doi.org/10.1109/ACCESS.2020.2990567

Brandt, P., Nuhnen, A., Lange, M., Möllmer, J., Weingart, O., & Janiak, C. (2019). Metal-Organic Frameworks with Potential Application for SO2 Separation and Flue Gas Desulfurization. *ACS Applied Materials and Interfaces*, *11*(19), 17350–17358. https://doi.org/10.1021/acsami.9b00029

Byron Bird, R., Stewart, W. E., & Lightfoot, E. N. (2002). *Transport Phenoma* (Wiley, Ed.; Second Edi).

Cadiau, A., Lee, J. S., Damasceno Borges, D., Fabry, P., Devic, T., Wharmby, M. T., Martineau, C., Foucher, D., Taulelle, F., Jun, C.-H., Hwang, Y. K., Stock, N., De Lange, M. F., Kapteijn, F., Gascon, J., Maurin, G., Chang, J.-S., & Serre, C. (2015). Design of Hydrophilic Metal Organic Framework Water Adsorbents for Heat Reallocation. *Advanced Materials*, *27*(32), 4775–4780. https://doi.org/https://doi.org/10.1002/adma.201502418

Calvin, K., Dasgupta, D., Krinner, G., Mukherji, A., Thorne, P. W., Trisos, C., Romero, J., Aldunce, P., Barret, K., Blanco, G., Cheung, W. W. L., Connors, S. L., Denton, F., Diongue-Niang, A., Dodman, D., Garschagen, M., Geden, O., Hayward, B., Jones, C., … Ha, M. (2023). *IPCC, 2023: Climate Change 2023: Synthesis Report, Summary for Policymakers. Contribution of Working Groups I, II and III to the Sixth Assessment Report of the Intergovernmental Panel on Climate Change [Core Writing Team, H. Lee and J. Romero (eds.)]. IPC* (P. Arias, M. Bustamante, I. Elgizouli, G. Flato, M. Howden, C. Méndez-Vallejo, J. J. Pereira, R. Pichs-Madruga, S. K. Rose, Y. Saheb, R. Sánchez Rodríguez, D. Ürge-Vorsatz, C. Xiao, N. Yassaa, J. Romero, J. Kim, E. F. Haites, Y. Jung, R. Stavins, … Y. Park, Eds.). https://doi.org/10.59327/IPCC/AR6-9789291691647.001

Chauvy, R., & De Weireld, G. (2020). CO2 Utilization Technologies in Europe: A Short Review. *Energy Technology*, *8*(12), 1–17. https://doi.org/10.1002/ente.202000627

Chue, K. T., Kim, J. N., Yoo, Y. J., Cho, S. H., & Yang, R. T. (1995). Comparison of Activated Carbon and Zeolite 13X for CO2 Recovery from Flue Gas by Pressure Swing Adsorption. *Industrial and Engineering Chemistry Research*, *34*(2), 591–598. https://doi.org/10.1021/ie00041a020

Costa, A., Coppitters, D., Dubois, L., Contino, F., Thomas, D., & De Weireld, G. (2024). Energy, exergy, economic and environmental (4E) analysis of a cryogenic carbon purification unit with membrane for

oxyfuel cement plant flue gas. *Applied Energy*, *357*, 122431. https://doi.org/10.1016/J.APENERGY.2023.122431

Costa, A., Henrotin, A., Heymans, N., Dubois, L., Thomas, D., & De Weireld, G. (2024). Multi-objective optimization of a hybrid carbon capture plant combining a Vacuum Pressure Swing Adsorption (VPSA) process with a Carbon Purification unit (CPU). *Chemical Engineering Journal*, *493*, 152345. https://doi.org/10.1016/J.CEJ.2024.152345

Damasceno Borges, D., Normand, P., Permiakova, A., Babarao, R., Heymans, N., Galvao, D. S., Serre, C., De Weireld, G., & Maurin, G. (2017). Gas Adsorption and Separation by the Al-Based Metal-Organic Framework MIL-160. *Journal of Physical Chemistry C*, *121*(48), 26822–26832. https://doi.org/10.1021/acs.jpcc.7b08856

Deb, K., & Jain, H. (2014). An Evolutionary Many-Objective Optimization Algorithm Using Reference-Point-Based Nondominated Sorting Approach , Part I : Solving Problems With Box Constraints. *IEEE Transactions on Evolutionary Computation*, *18*(4), 577–601. https://doi.org/10.1109/TEVC.2013.2281535

Deb, K., Pratap, A., Agarwal, S., & Meyarivan, T. (2002). A fast and elitist multiobjective genetic algorithm: NSGA-II. *IEEE Transactions on Evolutionary Computation*, *6*(2), 182–197. https://doi.org/10.1109/4235.996017

Decoste, J. B., Peterson, G. W., Schindler, B. J., Killops, K. L., Browe, M. A., & Mahle, J. J. (2013). The effect of water adsorption on the structure of the carboxylate containing metal-organic frameworks Cu-BTC, Mg-MOF-74, and UiO-66. *Journal of Materials Chemistry A*, *1*(38), 11922–11932. https://doi.org/10.1039/c3ta12497e

Ding, M., Flaig, R. W., Jiang, H. L., & Yaghi, O. M. (2019). Carbon capture and conversion using metal-organic frameworks and MOF-based materials. In *Chemical Society Reviews* (Vol. 48, Issue 10, pp. 2783–2828). Royal Society of Chemistry. https://doi.org/10.1039/c8cs00829a

Do, D. D. (1998). *Fundamentals of Diffusion and Adsorption in Porous Media* (Vol. 2). https://doi.org/10.1142/9781860943829_0007

Du, K. L., & Swamy, M. N. S. (2019). Neural networks and statistical learning, second edition. In *Neural Networks and Statistical Learning, Second Edition*. https://doi.org/10.1007/978-1-4471-7452-3

Edwards, M. F., & Richardson, J. F. (1968). Gas dispersion in packed beds. *Chemical Engineering Science*, *23*(2), 109–123. https://doi.org/10.1016/0009-2509(68)87056-3

Ergün, S. (1952). Fluid Flow Through Packed Columns. *Chemical Engineering Progress*, *48*.

Estupiñan Perez, L., Sarkar, P., & Rajendran, A. (2019). Experimental validation of multi-objective optimization techniques for design of vacuum swing adsorption processes. *Separation and Purification Technology*, *224*(March), 553–563. https://doi.org/10.1016/j.seppur.2019.05.039

Farmahini, A. H., Krishnamurthy, S., Friedrich, D., Brandani, S., & Sarkisov, L. (2021). Performance-Based Screening of Porous Materials for Carbon Capture. *Chemical Reviews*, *121*(17), 10666–10741. https://doi.org/10.1021/acs.chemrev.0c01266

Forrester, A. I. J., Sóbester, A., & Keane, A. J. (2008). Engineering Design via Surrogate Modelling. In *Engineering Design via Surrogate Modelling*. Wiley. https://doi.org/10.1002/9780470770801

Gaikwad, S., Kim, S. J., & Han, S. (2020). Novel metal–organic framework of UTSA-16 (Zn) synthesized by a microwave method: Outstanding performance for CO2 capture with improved stability to acid gases. *Journal of Industrial and Engineering Chemistry*, *87*, 250–263. https://doi.org/10.1016/j.jiec.2020.04.015

Grande, C. A. (2012). Advances in Pressure Swing Adsorption for Gas Separation. *ISRN Chemical Engineering*, *2012*, 1–13. https://doi.org/10.5402/2012/982934

Haghpanah, R., Majumder, A., Nilam, R., Rajendran, A., Farooq, S., Karimi, I. A., & Amanullah, M. (2013). Multiobjective optimization of a four-step adsorption process for postcombustion CO2 capture via finite volume simulation. *Industrial and Engineering Chemistry Research*, *52*(11), 4249–4265. https://doi.org/10.1021/ie302658y

Henrotin, A., Heymans, N., Duprez, M. E., Mouchaham, G., Serre, C., Wong, D., Robinson, R., Mulrooney, D., Casaban, J., & De Weireld, G. (2024). Lab-scale pilot for CO2 capture vacuum pressure swing adsorption: MIL-160(Al) vs zeolite 13X. *Carbon Capture Science & Technology*, *12*, 100224. https://doi.org/10.1016/j.ccst.2024.100224

Heymans, N., Duprez, M.-E., & De Weireld, G. (2021). MOF4AIR Project (H2020): Metal Organic Frameworks for Carbon Dioxide Adsorption Processes in Power Production and Energy Intensive Industries. *SSRN Electronic Journal*, *March*. https://doi.org/10.2139/ssrn.3821559

Hong, W. Y. (2022). A techno-economic review on carbon capture, utilisation and storage systems for achieving a net-zero CO2 emissions future. *Carbon Capture Science and Technology*, *3*(March), 100044. https://doi.org/10.1016/j.ccst.2022.100044

Hottel, H. C., Noble, J. K., Sarofim, A. F., Silcox, G. D., Wankat, P. C., & Knaebel, K. S. (2007). Heat and Mass Transfer. In D. W. Green (Ed.), *Perry's Chemical Enginners' handbook* (8th editio). McGraw-Hill.

Hu, Z., Wang, Y., Shah, B. B., & Zhao, D. (2019). CO 2 Capture in Metal–Organic Framework Adsorbents: An Engineering Perspective. *Advanced Sustainable Systems*, *3*(1), 1800080. https://doi.org/10.1002/adsu.201800080

IEA. (2020). Energy Technology Perspectives 2020 - Special Report on Carbon Capture Utilisation and Storage. *Energy Technology Perspectives 2020 - Special Report on Carbon Capture Utilisation and Storage*. https://doi.org/10.1787/208b66f4-en

Incropera, F. P., & DeWitt, D. P. (1996). *Fundamentals of Heat and Mass Transfer* (p. 890). https://doi.org/10.1016/j.applthermaleng.2011.03.022

Jiang, L., Fox, V. G., & Biegler, L. T. (2004). Simulation and optimal design of multiple-bed pressure swing adsorption systems. *AIChE Journal*, *50*(11), 2904–2917. https://doi.org/10.1002/aic.10223

Jin, R., Chen, W., & Sudjianto, A. (2005). An efficient algorithm for constructing optimal design of computer experiments. *Journal of Statistical Planning and Inference*, *134*(1), 268–287. https://doi.org/10.1016/j.jspi.2004.02.014

Karimi, M., Ferreira, A., Rodrigues, A. E., Nouar, F., Serre, C., & Silva, J. A. C. (2023). MIL-160(Al) as a Candidate for Biogas Upgrading and CO2 Capture by Adsorption Processes. *Industrial and Engineering Chemistry Research*, *62*(12), 5216–5229. https://doi.org/10.1021/acs.iecr.2c04150

Karimi, M., Siqueira, R. M., Rodrigues, A. E., Nouar, F., Silva, J. A. C., Serre, C., & Ferreira, A. (2024). Biogas upgrading using shaped MOF MIL-160(Al) by pressure swing adsorption process: Experimental

and dynamic modelling assessment. *Separation and Purification Technology*, *344*(March). https://doi.org/10.1016/j.seppur.2024.127260

Khurana, M., & Farooq, S. (2016a). Adsorbent Screening for Postcombustion CO2 Capture: A Method Relating Equilibrium Isotherm Characteristics to an Optimum Vacuum Swing Adsorption Process Performance. *Industrial and Engineering Chemistry Research*, *55*(8), 2447–2460. https://doi.org/10.1021/acs.iecr.5b04531

Khurana, M., & Farooq, S. (2016b). Simulation and optimization of a 6-step dual-reflux VSA cycle for post-combustion CO2 capture. *Chemical Engineering Science*, *152*, 507–515. https://doi.org/10.1016/j.ces.2016.06.033

Knox, J. C., Ebner, A. D., Levan, M. D., Coker, R. F., & Ritter, J. A. (2016). Limitations of Breakthrough Curve Analysis in Fixed-Bed Adsorption. *Industrial and Engineering Chemistry Research*, *55*(16), 4734–4748. https://doi.org/10.1021/acs.iecr.6b00516

Kreith, F., Manglik, R. M., & Bohn, M. S. (2011). *Principles of Heat Transfer* (Seventh). Cengage Learning. https://doi.org/10.1115/1.1497490

Krishnamurthy, S., Rao, V. R., Guntuka, S., Sharratt, P., Haghpanah, R., Rajendran, A., Amanullah, M., Karimi, I. A., & Farooq, S. (2014). CO 2 capture from dry flue gas by vacuum swing adsorption: A pilot plant study. *AIChE Journal*, *60*(5), 1830–1842. https://doi.org/10.1002/aic.14435

Kudela, J., & Matousek, R. (2022). Recent advances and applications of surrogate models for finite element method computations: a review. *Soft Computing*, *26*(24), 13709–13733. https://doi.org/10.1007/s00500-022-07362-8

Langmuir, I. (1918). The Adsorption of Gases on Plane Surfaces of Glass, Mica and Platinum. *Journal of the American Chemical Society*, *40*(9), 1361–1403. https://doi.org/10.1021/ja01269a066

Leperi, K. T., Yancy-Caballero, D., Snurr, R. Q., & You, F. (2019). 110th Anniversary: Surrogate Models Based on Artificial Neural Networks to Simulate and Optimize Pressure Swing Adsorption Cycles for CO2 Capture. *Industrial and Engineering Chemistry Research*, *58*(39), 18241–18252. https://doi.org/10.1021/acs.iecr.9b02383

Li, D., Zhou, Y., Shen, Y., Sun, W., Fu, Q., Yan, H., & Zhang, D. (2016). Experiment and simulation for separating CO2/N2 by dual-reflux pressure swing adsorption process. *Chemical Engineering Journal*, *297*, 315–324. https://doi.org/10.1016/j.cej.2016.03.075

Lin, J. Bin, Nguyen, T. T. T., Vaidhyanathan, R., Burner, J., Taylor, J. M., Durekova, H., Akhtar, F., Mah, R. K., Ghaffari-Nik, O., Marx, S., Fylstra, N., Iremonger, S. S., Dawson, K. W., Sarkar, P., Hovington, P., Rajendran, A., Woo, T. K., & Shimizu, G. K. H. (2021). A scalable metal-organic framework as a durable physisorbent for carbon dioxide capture. *Science*, *374*(6574), 1464–1469. https://doi.org/10.1126/science.abi7281

Liu, Z., Wang, L., Kong, X., Li, P., Yu, J., & Rodrigues, A. E. (2012). Onsite CO 2 capture from flue gas by an adsorption process in a coal-fired power plant. *Industrial and Engineering Chemistry Research*, *51*(21), 7355–7363. https://doi.org/10.1021/ie3005308

Lyu, P., & Maurin, G. (2021). H2S Stability of Metal-Organic Frameworks: A Computational Assessment. *ACS Applied Materials and Interfaces*, *13*(3), 4813–4822. https://doi.org/10.1021/acsami.0c21285

Martin, H. (1978). Low peclet number particle-to-fluid heat and mass transfer in packed beds. *Chemical Engineering Science*, *33*(7), 913–919. https://doi.org/10.1016/0009-2509(78)85181-1

Maruyama, R. T., Pai, K. N., Subraveti, S. G., & Rajendran, A. (2020). Improving the performance of vacuum swing adsorption based CO2 capture under reduced recovery requirements. *International Journal of Greenhouse Gas Control*, *93*(August 2019), 102902. https://doi.org/10.1016/j.ijggc.2019.102902

Masala, A., Vitillo, J. G., Mondino, G., Grande, C. A., Blom, R., Manzoli, M., Marshall, M., & Bordiga, S. (2017). CO2 capture in dry and wet conditions in UTSA-16 metal-organic framework. *ACS Applied Materials and Interfaces*, *9*(1), 455–463. https://doi.org/10.1021/acsami.6b13216

McKay, M. D., Beckman, R. J., & Conover, W. J. (1979). A Comparison of Three Methods for Selecting Values of Input Variables in the Analysis of Output from a Computer Code. *Technometrics*, *21*(2), 239. https://doi.org/10.2307/1268522

Mondal, M. K., Balsora, H. K., & Varshney, P. (2012). Progress and trends in CO2 capture/separation technologies: A review. *Energy*, *46*(1), 431–441. https://doi.org/10.1016/j.energy.2012.08.006

Myers, A. L., & Prausnitz, J. M. (1965). Thermodynamics of Mixed-Gas Adsorption. *A.I.Ch.E. Journal*, *11*(1), 121–127.

N.Borhani, T., & Wang, M. (2019). Role of solvents in CO2 capture processes: The review of selection and design methods. *Renewable and Sustainable Energy Reviews*, *114*(July), 109299. https://doi.org/10.1016/j.rser.2019.109299

NETL. (2023). *Point Source Carbon Capture from Industrial Sources*. *August*. https://netl.doe.gov/sites/default/files/2023-08/Program-160.pdf

Nguyen, T. T. T., Lin, J. Bin, Shimizu, G. K. H., & Rajendran, A. (2022). Separation of CO2 and N2 on a hydrophobic metal organic framework CALF-20. *Chemical Engineering Journal*, *442*(P2), 136263. https://doi.org/10.1016/j.cej.2022.136263

Nguyen, T. T. T., Shimizu, G. K. H., & Rajendran, A. (2023). CO2/N2 separation by vacuum swing adsorption using a metal–organic framework, CALF-20: Multi-objective optimization and experimental validation. *Chemical Engineering Journal*, *452*(P4), 139550. https://doi.org/10.1016/j.cej.2022.139550

Pai, K. N., Prasad, V., & Rajendran, A. (2021). Practically Achievable Process Performance Limits for Pressure-Vacuum Swing Adsorption-Based Postcombustion CO2Capture. *ACS Sustainable Chemistry and Engineering*, *9*(10), 3838–3849. https://doi.org/10.1021/acssuschemeng.0c08933

Pedregosa, F., Varoquaux, G., Gramfort, A., Michel, V., Thirion, B., Grisel, O., Blondel, M., Prettenhofer, P., Weiss, R., Dubourg, V., Vanderplas, J., Passos, A., Cournapeau, D., Brucher, M., Perrot, M., & Duchesnay, É. (2011). Scikit-learn: Machine Learning in Python. *Journal of Machine Learning Research*, *12*(85), 2825–2830. http://jmlr.org/papers/v12/pedregosa11a.html

Permyakova, A., Skrylnyk, O., Courbon, E., Affram, M., Wang, S., Lee, U. H., Valekar, A. H., Nouar, F., Mouchaham, G., Devic, T., De Weireld, G., Chang, J. S., Steunou, N., Frère, M., & Serre, C. (2017). Synthesis Optimization, Shaping, and Heat Reallocation Evaluation of the Hydrophilic Metal–Organic Framework MIL-160(Al). *ChemSusChem*, *10*(7), 1419–1426. https://doi.org/10.1002/cssc.201700164

Poling, B. E., Prausnitz, J. M., & O'Connell, J. P. (2001). *The properties of gases and liquids* (Fifth Edit). McGraw-Hill. https://pubs.aip.org/physicstoday/article/12/4/38/895367/The-Properties-of-Gases-and-Liquids

Raganati, F., Miccio, F., & Ammendola, P. (2021). Adsorption of Carbon Dioxide for Post-combustion Capture: A Review. *Energy & Fuels*, *35*(16), 12845–12868. https://doi.org/10.1021/acs.energyfuels.1c01618

Rajagopalan, A. K., Avila, A. M., & Rajendran, A. (2016). Do adsorbent screening metrics predict process performance? A process optimisation based study for post-combustion capture of CO2. *International Journal of Greenhouse Gas Control*, *46*, 76–85. https://doi.org/10.1016/j.ijggc.2015.12.033

Rasmussen, C. E., & Williams, C. K. I. (2005). *Gaussian Processes for Machine Learning*. The MIT Press. https://doi.org/10.7551/mitpress/3206.001.0001

Riboldi, L., & Bolland, O. (2017). Overview on Pressure Swing Adsorption (PSA) as CO2 Capture Technology: State-of-the-Art, Limits and Potentials. *Energy Procedia*, *114*(1876), 2390–2400. https://doi.org/10.1016/j.egypro.2017.03.1385

Ruthven, D. (1984). *Principles of Adsorption and Adsorption Processes* (First). John Wiley & Sons.

Severino, M. I., Gkaniatsou, E., Nouar, F., Pinto, M. L., & Serre, C. (2021). MOFs industrialization: A complete assessment of production costs. *Faraday Discussions*, *231*, 326–341. https://doi.org/10.1039/d1fd00018g

Shen, C., Liu, Z., Li, P., & Yu, J. (2012). Two-stage VPSA process for CO 2 capture from flue gas using activated carbon beads. *Industrial and Engineering Chemistry Research*, *51*(13), 5011–5021. https://doi.org/10.1021/ie202097y

Shen, C., Yu, J., Li, P., Grande, C. A., & Rodrigues, A. E. (2011). Capture of CO2 from flue gas by vacuum pressure swing adsorption using activated carbon beads. *Adsorption*, *17*(1), 179–188. https://doi.org/10.1007/s10450-010-9298-y

Sifat, N. S., & Haseli, Y. (2019). A critical review of CO2 capture technologies and prospects for clean power generation. *Energies*, *12*(21). https://doi.org/10.3390/en12214143

Silva, M. P., Ribeiro, A. M., Silva, C. G., Nogueira, I. B. R., Cho, K. H., Lee, U. H., Faria, J. L., Loureiro, J. L., Chang, J. S., Rodrigues, A. E., & Ferreira, A. (2021). MIL-160(Al) MOF's potential in adsorptive water harvesting. *Adsorption*, *27*(2), 213–226. https://doi.org/10.1007/s10450-020-00286-5

Spigarelli, B. P., & Kawatra, S. K. (2013). Opportunities and challenges in carbon dioxide capture. *Journal of CO2 Utilization*, *1*, 69–87. https://doi.org/10.1016/j.jcou.2013.03.002

Streb, A., & Mazzotti, M. (2022). Performance limits of neural networks for optimizing an adsorption process for hydrogen purification and CO2 capture. *Computers and Chemical Engineering*, *166*(August), 107974. https://doi.org/10.1016/j.compchemeng.2022.107974

Subraveti, S. G., Li, Z., Prasad, V., & Rajendran, A. (2019). Machine Learning-Based Multiobjective Optimization of Pressure Swing Adsorption. *Industrial and Engineering Chemistry Research*, *58*(44), 20412–20422. https://doi.org/10.1021/acs.iecr.9b04173

Tan, K., Zuluaga, S., Wang, H., Canepa, P., Soliman, K., Cure, J., Li, J., Thonhauser, T., & Chabal, Y. J. (2017). Interaction of Acid Gases SO2 and NO2 with Coordinatively Unsaturated Metal Organic Frameworks: M-MOF-74 (M = Zn, Mg, Ni, Co). *Chemistry of Materials*, *29*(10), 4227–4235. https://doi.org/10.1021/acs.chemmater.7b00005

Tolazzi, N., Steffani, E., Barbosa-Coutinho, E., Severo Júnior, J. B., Pinto, J. C., & Schwaab, M. (2018). Adsorption equilibrium models: Computation of confidence regions of parameter estimates. *Chemical Engineering Research and Design*, *138*, 144–157. https://doi.org/10.1016/j.cherd.2018.08.027

Versteeg, H. K., & Malalasekera, W. (2007). *An Introduction to Computational Fluid Dynamics* (Second edi). Pearson Education. http://www.ncbi.nlm.nih.gov/pubmed/6686412

Wahiduzzaman, M., Lenzen, D., Maurin, G., Stock, N., & Wharmby, M. T. (2018). Rietveld Refinement of MIL-160 and Its Structural Flexibility Upon H2O and N2 Adsorption. *European Journal of Inorganic Chemistry*, *2018*(32), 3626–3632. https://doi.org/10.1002/ejic.201800323

Wakao, N., & Kaguei, S. (1982). *Heat and Mass Transfer in Packed Beds*. Gordon and Breach Science Publishers.

Wang, L., Liu, Z., Li, P., Wang, J., & Yu, J. (2012). CO2 capture from flue gas by two successive VPSA units using 13XAPG. *Adsorption*, *18*(5–6), 445–459. https://doi.org/10.1007/s10450-012-9431-1

Wang, Z., Shen, Y., Zhang, D., Tang, Z., & Li, W. (2022). A comparative study of multi-objective optimization with ANN-based VPSA model for CO2capture from dry flue gas. *Journal of Environmental Chemical Engineering*, *10*(3), 108031. https://doi.org/10.1016/j.jece.2022.108031

Wilberforce, T., Olabi, A. G., Sayed, E. T., Elsaid, K., & Abdelkareem, M. A. (2021). Progress in carbon capture technologies. *Science of the Total Environment*, *761*, 143203. https://doi.org/10.1016/j.scitotenv.2020.143203

WMO. (2024). *WMO confirms 2024 as warmest year on record at about 1.55°C above pre-industrial level*. https://wmo.int/news/media-centre/wmo-confirms-2024-warmest-year-record-about-155degc-above-pre-industrial-level

Yagi, S., & Kunii, D. (1960). Studies on heat transfer near wall surface in packed beds. *AIChE Journal*, *6*(1), 97–104. https://doi.org/10.1002/aic.690060119

Yang, RalphT. (1987). Gas Separation by Adsorption Processes. In *Chemical Engineering Science* (Vol. 43, Issue 4). Elsevier. https://doi.org/10.1016/C2013-0-04269-7

Younas, M., Rezakazemi, M., Daud, M., Wazir, M. B., Ahmad, S., Ullah, N., Inamuddin, & Ramakrishna, S. (2020). Recent progress and remaining challenges in post-combustion CO2 capture using metal-organic frameworks (MOFs). *Progress in Energy and Combustion Science*, *80*. https://doi.org/10.1016/j.pecs.2020.100849

Yu, J., & Balbuena, P. B. (2013). Water Effects on Postcombustion CO 2 Capture in Mg-MOF-74. *The Journal of Physical Chemistry C*, *117*(7), 3383–3388. https://doi.org/10.1021/jp311118x

Yu, X., Liu, B., Shen, Y., & Zhang, D. (2022). Design and experiment of high-productivity two-stage vacuum pressure swing adsorption process for carbon capturing from dry flue gas. *Chinese Journal of Chemical Engineering*, *43*, 378–391. https://doi.org/10.1016/j.cjche.2021.02.022

Declaration of interests

☒ The authors declare that they have no known competing financial interests or personal relationships that could have appeared to influence the work reported in this paper.

☐ The authors declare the following financial interests/personal relationships which may be considered as potential competing interests:

Highlights

- Simulation model development for 3-bed 6-step VPSA cycle.
- Model validation at lab scale – deviation: 1.47% for purity and 3.19% for recovery.
- Pareto front obtained with ANN model is equivalent to the one obtained with Aspen.
- Industrial VPSA pilot simulated can reach 95% purity and recovery.
-